Journal of Geophysical Research: Planets

RESEARCH ARTICLE
10.1029/2017JE005463

Key Points:
- Impact velocity and target properties largely affect simple crater morphology in layered targets
- Lunar regolith thicknesses inferred from crater morphometry deviate up to 80% from previous estimates
- The morphological transition from normal to flat-bottomed craters is the most robust indicator for the thickness of the uppermost layer

Supporting Information:
- Supporting Information S1
- Data Set S1
- Data Set S2

Correspondence to:
N. C. Prieur,
nilscp@geo.uio.no

Citation:
Prieur, N. C., Rolf, T., Wünnemann, K., & Werner, S. C. (2018). Formation of simple impact craters in layered targets: Implications for lunar crater morphology and regolith thickness. *Journal of Geophysical Research: Planets*, *123*, 1555–1578. https://doi.org/10.1029/2017JE005463

Received 5 OCT 2017
Accepted 27 MAY 2018
Accepted article online 5 JUN 2018
Published online 29 JUN 2018

Formation of Simple Impact Craters in Layered Targets: Implications for Lunar Crater Morphology and Regolith Thickness

N. C. Prieur[1], T. Rolf[1], K. Wünnemann[2,3], and S. C. Werner[1]

[1]Centre for Earth Evolution and Dynamics, University of Oslo, Oslo, Norway, [2]Museum für Naturkunde, Leibniz-Institute for Evolution and Biodiversity Science, Berlin, Germany, [3]Institute of Geological Sciences, Planetary Sciences and Remote Sensing, Freie Universität Berlin, Berlin, Germany

Abstract Impact crater morphologies vary significantly across the lunar maria. Craters with diameter less than 400 m are closely related to variations in target properties (rock strength, porosity, and layering) as well as the impact velocity. Here we investigate target and impact conditions feasible for reproducing crater morphologies, such as normal, central-mound, flat-bottomed, and concentric craters, using numerical models of impact crater formation in two-layer targets under lunar conditions (i.e., average-impact velocity and gravity). Based on more than 1,000 numerical models, we observe that concentric craters can form with a strength contrast as low as factor of 2 between the layers as long as the difference in cohesion is larger than a value between 50 and 450 kPa (for an impact velocity of 12.7 km/s). Because of this small contrast, concentric craters do not serve as a good indication for the lunar regolith-mare interface. Crater morphology changes with crater diameter according to three different scenarios depending on layers' strengths and the impact velocity. For high-impact velocity or/and moderate material strength, normal crater morphology transitions directly to concentric morphology, while with large material strengths and/or low-impact velocity, craters change with size from normal to flat-bottomed and then to concentric morphology; only this latter pathway is consistent with previous laboratory results. Lunar regolith thicknesses estimated from crater morphologies can differ by up to 80% from previously inferred thicknesses. The transition from normal to flat-bottomed craters is found to be the most robust transition to infer the thickness of the surficial target layer.

1. Introduction

The surface of the Moon shows great shape variety across its small simple impact crater population. Craters on the lunar maria with rim-to-rim diameters less than 400 m exhibit either bowl-shaped (denoted as normal crater, NC; Figure 1a), central-mound (CMC; Figure 1b), flat-bottomed (FBC; Figure 1c), or concentric (CC; Figure 1d) morphologies (Gault et al., 1966; Oberbeck & Quaide, 1967). These different morphologies have been reproduced in laboratory impact experiments with targets composed of two layers with different properties (Quaide & Oberbeck, 1968): an upper layer representative of the lunar regolith on top of more competent basement rocks. Therefore, the presence of a property discontinuity (in strength and density) in the near-surface stratigraphy has been suggested to cause the variety of observed crater morphologies (Oberbeck & Quaide, 1967; Quaide & Oberbeck, 1968). Moreover, the laboratory experiments revealed a relation between simple crater morphology, crater diameter, and the uppermost layer thickness (D_{RIM}/T, with rim-to-rim crater diameter D_{RIM} and uppermost layer thickness T): crater morphology transitions from one geometry to the other at constant D_{RIM}/T, independent of impactor velocities or impact angles. Furthermore, the strength of the lower layer influences the results only slightly (Quaide & Oberbeck, 1968) (henceforth Q&O). Accordingly, Q&O found that NCs form for $D_{RIM}/T \leq 4$, CMCs and FBCs for $4 < D_{RIM}/T \leq$ 8–10, and CCs for 8–10 $< D_{RIM}/T < X$, where X may be as large as 20. For even greater D_{RIM}/T, the uppermost layer does not have significant effects anymore, such that NCs are the dominant morphology. The relationship between morphological transitions and D_{RIM}/T has been used to estimate the thickness of the lunar regolith (e.g., Fa et al., 2014, Oberbeck & Quaide, 1967, 1968). Among such studies, Oberbeck and Quaide (1968) estimated from crater morphologies measured at 12 sites on the lunar maria and interior of craters that the lunar regolith thickness ranges from 3.3 to 16 m. They suggested that these different regolith thicknesses reflect different time spans between the emplacement of volcanic lava flows and formation of the impact crater.

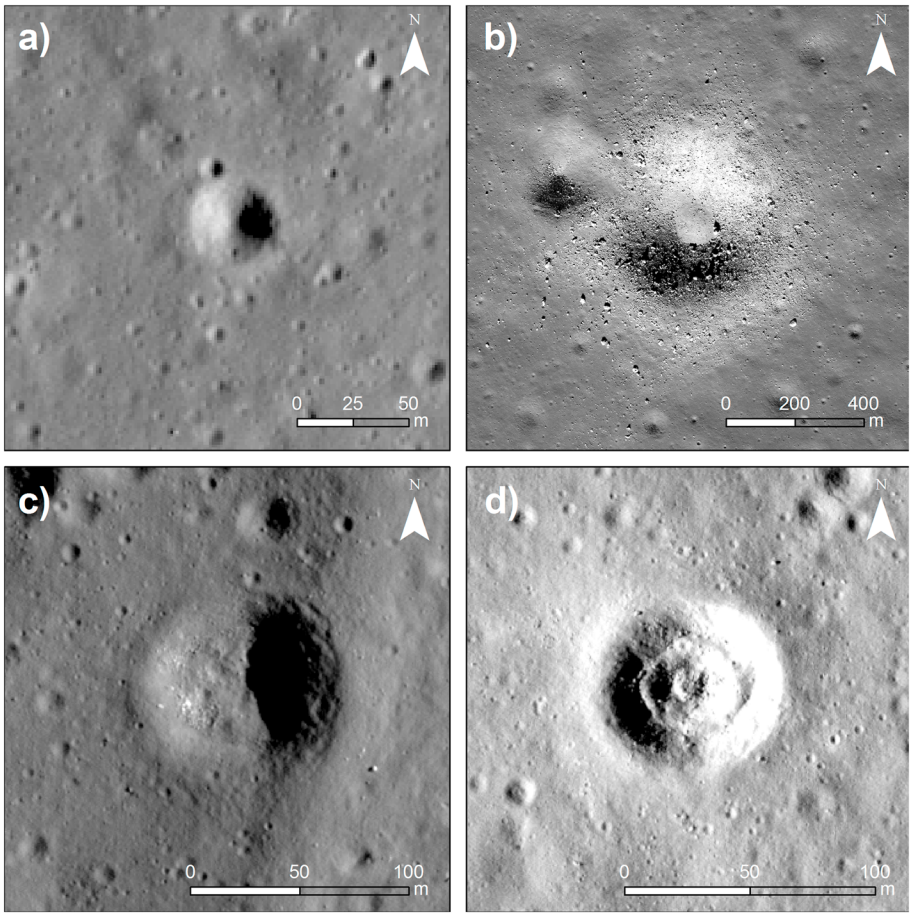

Figure 1. Examples of NAC (Narrow Angle Camera aboard the Lunar Reconnaissance Orbiter) images showing (a) normal (16.94°N, 60.01°E), (b) central-mound (58.96°N, 8.12°W), (c) flat-bottomed (19.69°S, 127.17°E), and (d) concentric (14.56°N, 57.57°E) crater morphologies on the lunar maria [NASA/GSFC/Arizona State University].

Above estimates, however, assume that the strength discontinuity causing the different crater morphologies is always the regolith-mare interface. This interface is represented in laboratory experiments by two homogeneous layers, even though the lunar regolith is known to be highly heterogeneous and most likely consisting of multiple interlayers of fine- and coarse-grained debris (see Wilcox et al., 2005, for more information). Large thickness variations are expected over relatively small distances as a function of topography and local production of regolith (Wilcox et al., 2005). Moreover, the boundary between the regolith and the substrate bedrock may not be distinct but may transition more gradually from granular and porous to fractured and weakened basalt (Mahanti et al., 2017; Stopar et al., 2017; Wilcox et al., 2005). As the required strength or density difference between layers and the near-surface stratigraphy to produce such craters are still unknown, it also remains unclear which strength discontinuity may actually cause CMC, FBC, and CC to form. Consequently, current interpretations of previous laboratory-scale experiments with regard to lunar regolith thickness estimates have to be considered with care and additional experiments, also in the form of numerical simulations seem necessary. While prone to its own limitations (section 2.1), numerical modeling of the crater formation process in layered targets helps to refine relationships between observed simple crater morphologies, target properties, and impactor velocities (e.g., Senft & Stewart, 2007) and to identify the governing physical processes in the subsurface upon the impact event.

In the present work, we study the effect of target layering on the Moon using a simple numerical model with a two-layer setup similar to the laboratory experiments of Q&O because (i) information about target layering and properties are still poorly known, (ii) our knowledge on the influence of a simple two-layer crater formation mechanism and transition in crater morphologies is still limited, and (iii) crater morphologies such as CCs with multiple inner cavities are almost absent, indicating that simplifying the near-surface stratigraphy

to two layers may be reasonable. We define the term "regolith" as in Oberbeck et al. (1973), where a classic mare regolith is "not just the reworked surface layer, but is the entire blanket of rock debris overlying cohesive substrate rocks." By using such numerical model setup we can only simulate abrupt transitions such as (possibly) between the bottom of the regolith and the underlying bedrock, interlayers of reworked fine-grained materials, and/or coarser grained debris within the regolith. We search for target parameters suitable to form simple craters with CMC, FBC and CC shape. The role of target (strength and porosity) and impactor properties (projectile diameter and velocity) is studied over a wide range of parameters applicable to the Moon.

2. Methods

2.1. Numerical Simulations of Crater Formation in Layered Targets

Impact cratering in layered media in two dimensions is investigated using the hydrocode iSALE-2D (iSALE-Chicxulub release), which is based on the SALE (Simplified Arbitrary Lagrangian Eulerian) hydrocode solution algorithm (Amsden et al., 1980). In the 1990s, Melosh et al. (1992) and Ivanov et al. (1997) improved the SALE hydrocode by including equations of state, multiple materials, a fragmentation, and an elasto-plastic constitutive model. More recent material model modifications include the addition of a compaction model (Collins et al., 2011; Wünnemann et al., 2006), the combination of both damage (i.e., the amount of fragmentation) and deformation in a more sophisticated strength model (Collins et al., 2004), and the integration of the effect of dilatancy (Collins, 2014).

We extended our previous setup (Prieur et al., 2017) to a simple sharp two-layer setup to investigate the effects of target layering on the development of crater morphologies; each layer is assumed to be internally homogeneous. The strength of the layers and strength differences in between them are described by the Drucker-Prager strength model, $Y = \min(Y_0 + f\,p; Y_{LIM})$, which requires only three input strength parameters: the shear strength at zero pressure Y_0 (i.e., the cohesion), the limiting strength at high pressure Y_{LIM}, and the coefficient of friction f. The confining pressure p is self-consistently computed by iSALE. An important limitation of the Drucker-Prager strength model is that it neglects the strength degradation due to fracturing (Collins et al., 2004) and is most adequate to describe the resistance of granular and brecciated materials to shear deformation. The presence of material porosity is described by the ε-α compaction model (Collins et al., 2011; Wünnemann et al., 2006). Compaction model parameters other than the preimpact porosity of the target are here held constant at values that provide a reasonable fit to porous geological materials with initial porosity $\phi >$ ~10–15% (Collins et al., 2011; Prieur et al., 2017).

One limitation of our model setup is that we neglect dilatancy (i.e., bulking of materials under shear pressure), which may be important to reproduce accurately the large amount of collapse observed for some terrestrial simple craters (Collins, 2014). By ignoring dilatancy, our model may not accurately capture crater collapse. On the other hand, two technical advantages arise for our purposes: First, a strength model including dilatancy implies that target strength is dependent on both dilatancy and compaction model parameters (Collins, 2014) and omitting dilatancy thus allows us to separate the influences of strength and porosity on crater morphologies. Second, without dilatancy, the number of free model parameters is significantly reduced.

As we focus on simple craters, the crater collapse is dominated by slope failure (Melosh, 1977); hence, the effect of acoustic fluidization is omitted in our calculations. For all cases, we describe the thermodynamic state of the projectile and target layers with the ANEOS tabulated equation of state for basalt (Pierazzo et al., 2005). Thus, the effect of density contrasts in layered targets is here only investigated through varying the initial porosity of layers. The influence of target materials with different densities will be the subject of future investigations.

The accurate representation of a material interface between two layers is numerically challenging due to several reasons: First, the simulation of small craters ($D_{RIM} < 400$ m) is computationally very expensive, because of the relatively high cratering efficiency (i.e., the ratio between crater and projectile size; Holsapple, 1993). As a consequence, a greater number of cells are required to resolve both the relatively small projectile and the much larger resulting crater at sufficient resolution; hence, the computation time is significantly longer than in crater formation models with lower cratering efficiency. Second, the cell

Table 1
Target Parameters and Impactor Properties for the Different One- and Two-Layer Simulations Conducted in This Study

	Upper layer			Lower layer				
ID	f	Φ (%)	Cohesion (MPa)	f	Φ (%)	Cohesion (MPa)	Impact velocity (km/s)	Figure
Lower layer strength								
SL-1[a]	0.6	10	0.05	0.6	10	0.1	12.7	6, 11
SL-2[b]	0.6	10	0.05	0.6	10	0.5	12.7	6, 11
SL-3[c]	0.6	10	0.05	0.6	10	1.0	12.7	6, 11
SL-4[c]	0.6	10	0.05	0.6	10	5.0	12.7	6, 11
SL-5[c]	0.6	10	0.10	0.6	10	1.0	12.7	4d–4f, 5, 6, 11
SL-6[c]	0.6	10	0.10	0.6	10	20.0	12.7	6, 11
SL-7[c]	0.6	10	0.10	0.6	10	50.0	12.7	6, 11
SL-8[c]	0.6	10	0.10	0.6	10	100.0	12.7	6, 7a–7c, 11
Upper layer strength								
SU-1[c]	0.6	10	0.00	0.6	10	1.0	12.7	3d–3f, 6, 9a–9c
SU-2[d]	0.6	10	0.50	0.6	10	1.0	12.7	6
SU-3[c]	0.6	10	0.10	0.2	10	1.0	12.7	6, 9d–9f, 10
SU-4[c]	0.5	10	0.10	0.4	10	1.0	12.7	6
SU-5[c]	0.4	10	0.10	0.5	10	1.0	12.7	6
SU-6[c]	0.6	10	0.10	0.6	10	1.0	12.7	4d–4f, 5, 6
Impact velocity								
IV-1[c]	0.6	10	0.10	0.6	10	1.0	5.0	6, 11
IV-2[c]	0.6	10	0.10	0.6	10	1.0	7.5	6, 11
IV-3[c]	0.6	10	0.10	0.6	10	1.0	12.7	4d–4f, 5, 6, 11
Upper layer porosity								
PU-1[c]	0.6	30	0.10	0.6	10	1.0	12.7	4d–4f, 5, 6, 11
PU-2[c]	0.6	20	0.10	0.6	10	1.0	12.7	6, 11
PU-3[c]	0.6	10	0.10	0.6	10	1.0	12.7	6, 11
Homogeneous								
HO-1[e]	0.6	10	1.00	0.6	10	1.0	12.7	3a–3c, 6
Low-velocity impact and large lower layer strength								
SE-1[c]	0.6	10	0.10	0.6	10	100.0	1.0	6, 7d–7f, 8
Large strength contrast (gravity- over gravity-regime)								
GG-1[a]	0.6	10	5.0e-4	0.6	10	5.0e-2	12.7	4a–4c, 6

Note. Figures related to the different cases are specified.
[a]Gravity-dominated in both upper and lower layers. [b]Gravity-dominated upper layer over lower layer in the transitional regime. [c]Gravity-dominated upper layer over strength-dominated lower layer. [d]Strength-dominated in both upper and lower layers. [e]Strength-dominated one layer.

size in iSALE-2D depends on both the number of cells per projectile radius (*CPPR*) and on the size of the projectile. Finally, we estimate that a minimum of 10 numerical grid cells is required to resolve the influence of the uppermost layer properly. Typical estimates of lunar maria regolith thickness range from 2 to 10 m (Fa et al., 2014; Fa & Jin, 2009; McKay et al., 1991; Oberbeck & Quaide, 1968), and the combination of such a thin layer and the high cratering efficiencies of small impacts results in computational costs that do not allow a detailed sensitivity analysis where several hundreds of models have to be conducted. To achieve an acceptable balance between model resolution (*CPPR* = 20) and computation time, most of our simulations have been carried out on a larger scale (i.e., lower cratering efficiency for a constant impact velocity) than expected for the lunar surface. To do this, a rather thick upper layer (T = 400 m) is chosen, while impact velocity (U = 12.7 km/s) and surface gravity (g = 1.62 m/s^2) are held constant in most cases. As the upper layer is thus thicker than estimated for typical regolith, bigger projectile diameters L = 70–1,500 m are required to investigate transitions in crater morphology with increasing crater diameter, which leads to a large range of relative thicknesses $\sim 4 \leq D_{RIM}/T \leq \sim 40$. Moreover, as we use a thicker upper layer, the strength values expected for the lunar maria or other interlayers $T \sim$ 1–10 m, need to be scaled up to T = 400 m. This step is here done based on strength properties of damaged- and intact-basalt derived at laboratory scale (Schultz, 1995; see supporting information S1). A shortcoming of our approach is thus that cratering efficiency is decreased by 2 to 3 times. To evaluate how higher crater efficiency affects our results, we also computed some cases with thinner upper layers (T = 200 m and T = 50 m; see supporting information S2). In such cases,

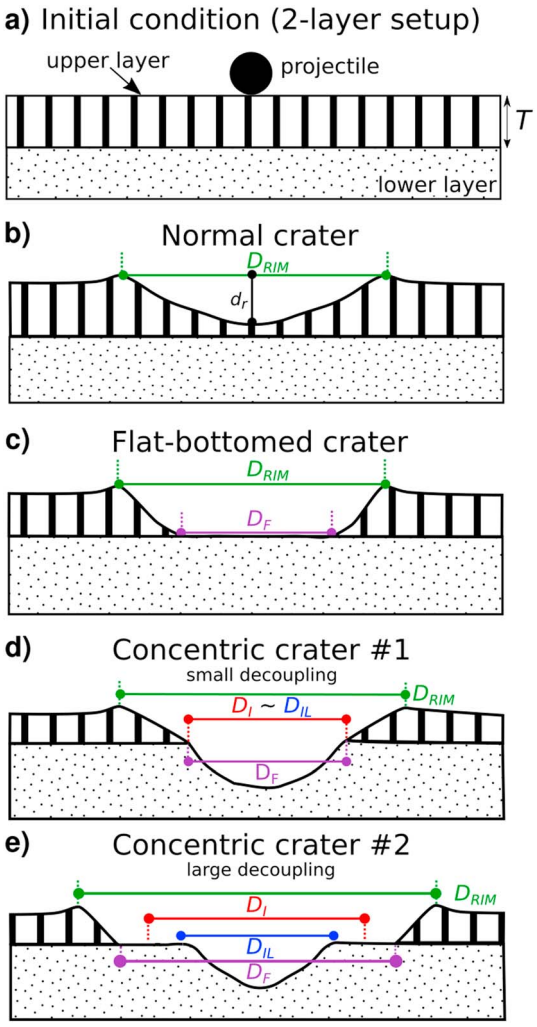

Figure 2. Schematic description of (a) the initial condition for the sharp two-layer model and of the most important measured parameters for (b) normal, (c) flat-bottomed, and (d and e) concentric craters. See main text for definition of D_{RIM}, D_I, D_{IL}, D_F, and d_R. More information about CMCs can also be found in section 2.3.

D_{RIM}/T tends to increase for higher cratering efficiency. However, this shift in D_{RIM}/T is minimal (on average less than 5%), so that our results should also be applicable for thinner upper layers.

2.2. Performed Simulations

Depending on the impactor and target properties, crater formation can either be strength- or gravity-dominated (Holsapple & Schmidt, 1982; Schmidt, 1980; Schmidt & Housen, 1987). In the former case, the strength of the target controls crater growth, while gravity of the target body is the dominating force in the latter case. To investigate the conditions required to form concentric and other simple crater morphologies, we thus consider all scenarios possible in our two-layer setup (see Table 1): (1) a gravity-dominated upper layer overlies a strength-dominated lower layer (e.g., cases SU-1 and SU-3), which describes well a loose upper layer on the top of a fractured or intact bedrock; (2) a strength-dominated layer over a strength-dominated layer (case SU-2), such as strong interlayers of cohesive materials within the basaltic mare; (3) a gravity-dominated over another gravity-dominated layer (case GG-1), which could represent interlayers within the regolith. The scenario of a strength-dominated upper layer whose strength overcomes that of the lower layer is not taken into account here since we consider it as uncommon for the Moon. However, we consider (4) a strength-dominated homogeneous one-layer target (case HO-1) as an end-member case.

The strength contrast between material layers is varied either via the coefficient of friction f or via the cohesion Y_0 (Table 1). Because of the poorly constrained lunar target strength at planetary scale and the substantial regional variation of target properties (e.g., Fassett, 2016; Kiefer et al., 2012; Wieczorek et al., 2013), we tested a large range of strength values and strength contrasts (with a factor of 2–1,000) to infer a minimum strength contrast required to produce the crater morphologies defined above. Strength conditions appropriate for the Moon should be within the range of strength values tested here. We also investigate the effect of impactor velocity (e.g., IV-1–IV-3 and SE-1, U = 1.0–12.7 km/s) and of the uppermost layer's initial porosity ϕ (e.g., PU-1–PU-3, ϕ = 10–30%) to cover the range of realistic porosities suggested for the lunar crust and regolith (ϕ = 12% and $\leq$ 40%, respectively; see Slyuta, 2014; Wieczorek et al., 2013).

2.3. Classification and Measure of Crater Morphology and Geometry

All simulations are run until the final crater is formed, that is, including the gravity-driven collapse of the over-steepened transient crater wall and the formation of the breccia lens inside the crater. The final crater diameter is measured from rim-to-rim (denoted as rim-to-rim crater diameter D_{RIM}; Figure 2b). A crater is defined as FBC when the length of its flat floor is at least 40% of its rim-to-rim crater diameter (Figure 2c). For CC, the inner crater rim may not have a local topographic high (e.g., Figures 3d and 3e). In order to work around this problem, we define craters to be concentric when we observe an abrupt decrease in slope angle of at least 20° along the cavity wall. The inner crater diameter (D_I) is measured from where the bend in the cavity wall slope is detected (Figure 2d). For particular cases where the ledge of the CCs is large and flat, D_I is defined at the midpoint of this long, flat ledge (Figure 2e). Note that our definition of D_I may differ from Q&O's (denoted here as D_{IL} and defined as the apparent diameter of the inner crater). For small decoupling, D_I and D_{IL} are more likely to be equal (Figure 2d). However, for large decoupling, we argue that some differences may happen if D_{IL} corresponds to the local topographic-high associated with the inner crater rim (Figure 2e). Q&O also defined an additional measure to characterize

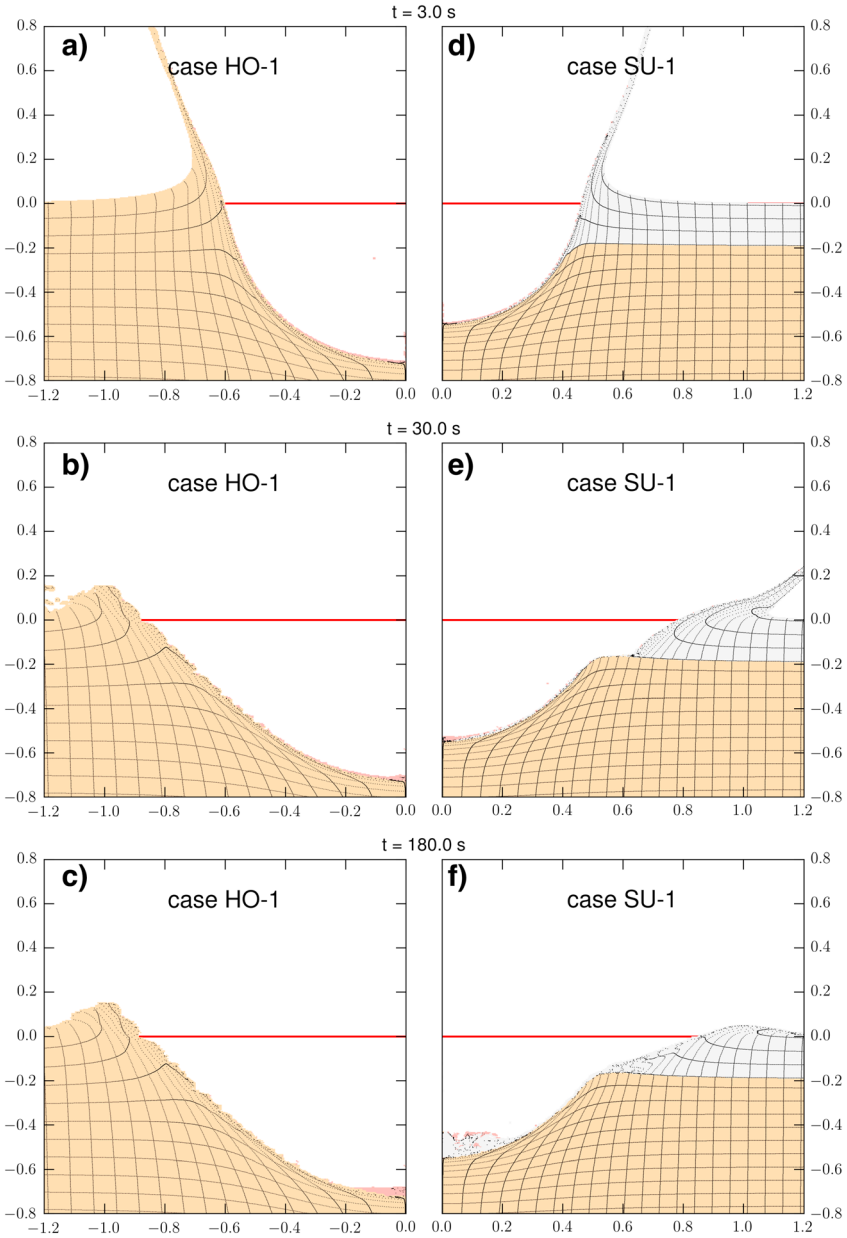

Figure 3. Snapshots of simple crater evolution for an asteroid impact with L = 250 m and U = 12.7 km/s into (a–c) a homogeneous target (Table 1, case HO-1) and (d–f) a two-layer target (Table 1, case SU-1). For both cases, f = 0.6 and Φ = 10%. Different colors represent materials with different cohesion (grey: Y_0 = 5 Pa; orange: Y_0 = 1.0 MPa; red: projectile). The horizontal and vertical black lines represent the deformation of the materials during crater formation. The red horizontal line denotes the preimpact surface. The x and y axis units are normalized to the final crater radius to the rim for each case.

the decoupling of layers, namely, the crater floor widths D_F (= the ledge's length + the inner crater diameter D_{IL}). Finally, a crater is classified to have a central mound if there is a central mound in the center of the crater.

2.4. Comparison of Modeled and Observed Lunar Concentric Craters

For the comparison between modeled CCs and observed lunar CCs (in section 4), we used high-resolution NAC images (Narrow Angle Camera) from the Lunar Reconnaissance Orbiter Camera (Robinson et al., 2010). For each case, NAC images with similar illumination angles (θ = 23–30° measured from the surface; see Table S3) are selected to avoid possible bias due to illumination conditions (e.g., Fa et al., 2014,

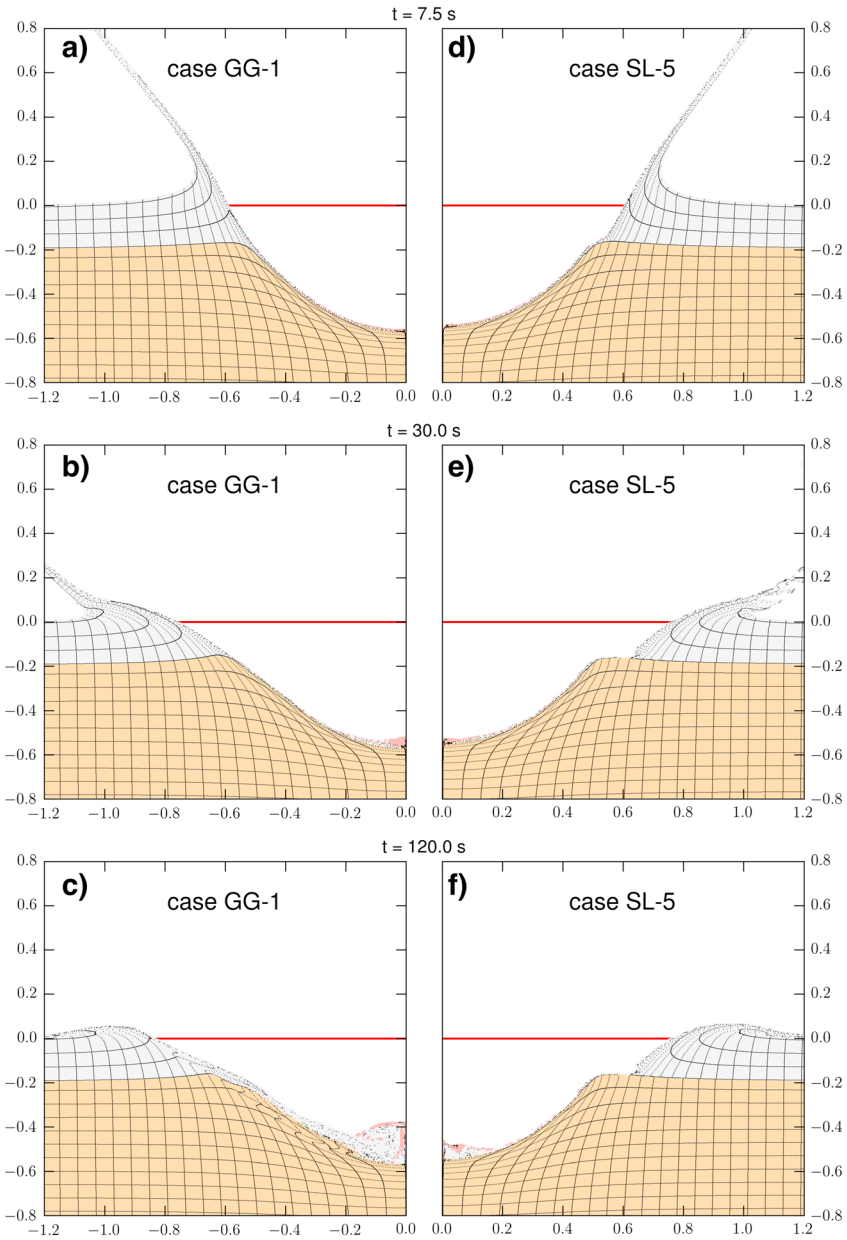

Figure 4. As in Figure 3 but for cases (a–c) GG-1 with 100× strength contrast between the layers representing the gravity-over gravity-dominated crater regime and (d–f) SL-5 with 10× strength contrast representing the gravity- over strength-dominated regime.

Oberbeck & Quaide, 1967, 1968). About 100 CCs are analyzed on Mare Crisium, Oceanus Procellarum, and Mare Tranquillitatis. Both the inner crater and rim-to-rim diameters are measured with the help of the CraterTools extension of ArcMap (Kneissl et al., 2011). The CraterTools allows three points along each crater rim to be specified, and an ellipse to be automatically fitted through those points. CCs are selected if their rim-to-rim crater diameters are larger than 25 m (i.e., they cover at least 25–50 pixels in the NAC image) and if we can clearly discern an inner cavity within the potential CCs, regardless of their degrees of freshness. As crater diameter degrades much slower than crater depth (e.g., Fassett & Thomson, 2014), we argue that this method of classification to sufficiently robust. Altogether, we estimate the uncertainty in the estimated inner and rim-to-rim crater diameters to be ±3 times the image resolution based on the inaccuracy in the measuring technique.

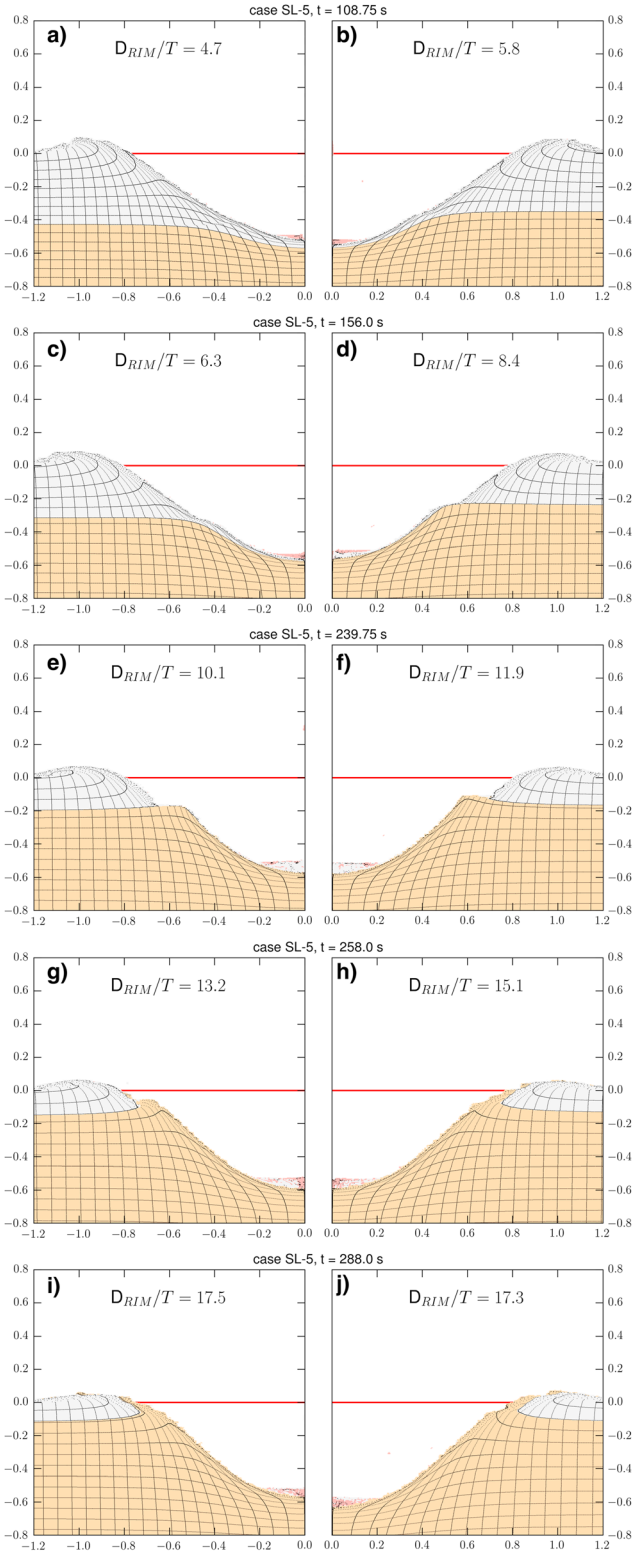

Figure 5. Final crater shapes for impacts with varying projectile diameter: (a) L = 100, (b) 130, (c) 150, (d) 200, (e) 250, (f) 300, (g) 350, (h) 400, (i) 450, and (j) 500 m. For all cases U = 12.7 km/s, f = 0.6, and Φ = 10%, Y_0 = 0.1 MPa (upper) and Y_0 = 1.0 MPa (lower), case SL-5. The ratio of the rim-to-rim diameter and the thickness of the upper layer (D_{RIM}/T) are specified in each subfigure. Other figure details are as in Figures 3 and 4.

To extend the comparison to observations, we also investigate the vertical crater dimensions, such as the depth and the height of ledges above the crater floor. A digital terrain model (NAC_DTM_M1113751844_M111375894, derived by the Arizona State University LROC team) was used (Brown et al., 2017). The NAC DTM has a coarser horizontal resolution (approximately about 5 times) than the original pair of NAC images and a vertical accuracy of about a meter. Because of that, the cross section of only a single fresh lunar CC with D_{RIM} = 185 m on Mare Crisium was found to reasonably resolve the topography of the inner crater. This crater was deemed to be fresh based on the large number of boulders present on the ejecta blanket. Finally, we compared our results to the geological cross section of one terrestrial CC formed by a large explosion experiment (PRE-MINE THROW-IV 6; Roddy, 1977). About 50 elevation points are extracted along the cross section of the 25-m crater.

3. Results

The evolution of crater morphology as a function of crater diameter is computed for the cases presented in Table 1. In the following, we describe separately the crater formation as a function of crater diameters for CCs (section 3.1), FBCs (section 3.2), and CMCs (section 3.3).

3.1. CC

Figures 4 and 5 show snapshots of crater growth for the impact of an asteroid with a diameter L = 250 m into four different target settings. For this projectile diameter, the previously known range of relative thicknesses ($9 < D_{RIM}/T < 20$; Q&O) suggests that a CC should form. During the excavation stage, the crater evolution in layered targets resembles the crater evolution in homogenous targets independent of whether the target is in fact homogeneous or has a more complex structure (Figures 4a/4d and 5a/5d). When the maximum crater depth is reached for the two-layered targets, different excavation flow and modification processes in the upper and lower layers are observed, which lead to a certain degree of decoupling between both layers. The strongest decoupling is observed for the layered target cases SL-5 and SU-1, because in these cases, the strength of the upper layer is much lower than the underlying layer. In all settings, the crater collapses subsequently, which typically takes 5–10 times the transient crater formation time, that is, the time when the cavity reaches its maximum volume. The degree of collapse is dependent on the strength properties of the layers and whether collapse occurs in the strength- or in the gravity-controlled regime (Figures 4d–4f and 5). In case SU-1, for example, the upper layer is gravity-controlled and target material moves inward along the cavity wall and slowly fills the inner cavity. This increases the thickness of the breccia lens at the crater floor and decreases the apparent crater depth (Figure 3f). The collapse of the upper layer ceases once the slope of the cavity wall reaches its angle of repose. For the other gravity-strength setup (SL-5), instead, the collapse is controlled by the greater resistance of the material against gravity forces (Figure 4f). In this case we observe both a distinct concentric morphology and a smaller collapse.

Although a strength contrast is present in cases GG-1 (100×; Figures 4a–4c) and SL-5 (10×; Figures 4d–4f), a CC forms only for

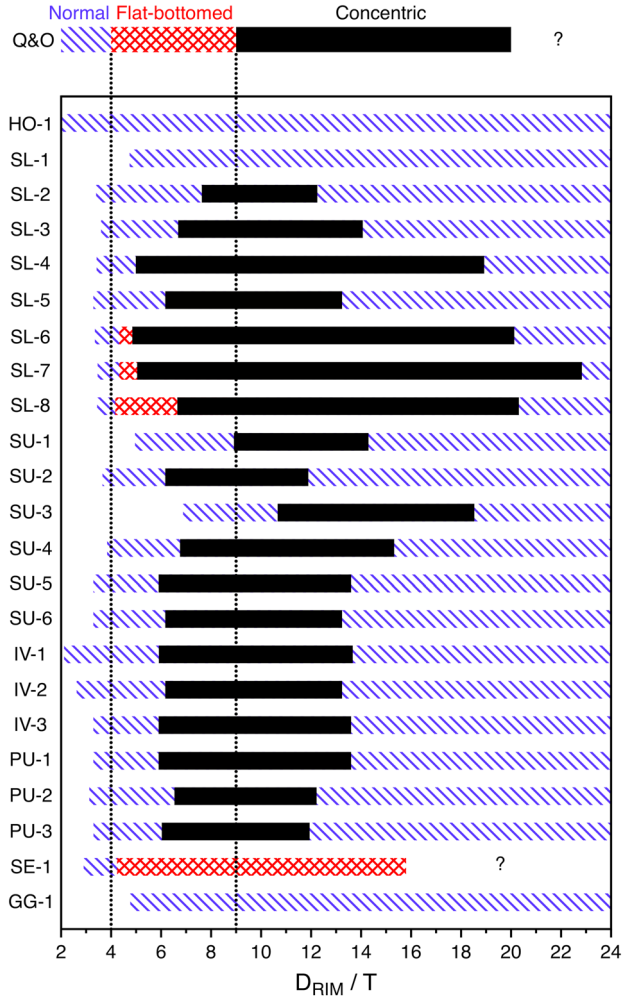

Figure 6. Detected crater morphologies as a function of the relative thickness D_{RIM}/T for varying projectile diameters L = 70–1,500 m in numerical simulations with target properties as summarized in Table 1. The top row labeled with "Q&O" provides a comparison to the work of Quaide and Oberbeck (1968). In case SE-1 large projectile diameters were needed because of the low crater efficiency. For $D_{RIM}/T > 16$, no results can be reported because the upper layer is represented by less than 10 grid cells (see section 2.1).

SL-5, whereas neither a decoupling between the layers nor the formation of a CC interior is observed for GG-1. These two cases differ only in their strength properties and in their cratering regimes. The absence of CC in the GG-1 case is likely due to the minimal difference in cohesion between the upper and lower layers (ΔY_0 = 0.045 MPa compared to ΔY_0 = 0.9 MPa for SL-5). Thus, CCs may form only if the difference in material strength is sufficient enough (see bullet point 1 in the list below for quantification).

Figure 5 depicts the final crater diameter for simulations in which we varied the projectile diameter (L = 70–1,500 m) for one target (SL-5). For increasing projectile diameters, crater morphology changes from normal bowl-shaped to concentric at $D_{RIM}/T \sim 6.2$ and back again to normal at $D_{RIM}/T > 13.2$. The decoupling between the upper and lower layer becomes more pronounced first (Figures 5a–5e), but then vanishes (Figures 5f–5h) as crater morphology returns from CC back to NC. As D_{RIM}/T increases, the originally flat-lying ledge, a characteristic of CCs, is lifted and tilted upward (Figures 5c and 5d) and eventually forms a sharp rim (Figures 5e and 5f). At $D_{RIM}/T \geq \sim 13$, material from the lower layer is incorporated in the ejecta blanket (i.e., material of the lower layer covers parts of the upper layer).

Based on the different target settings (Table 1) and varied projectile sizes (implying different relative upper layer thickness) summarized in Figure 6, we find the following:

1. CCs can form for strength contrasts between the layers as low as 2 (case SU-2) and as large as 1,000 (case SL-8). This is true for U = 12.7 km/s and as long as the difference in cohesion ΔY_0 between layers is greater than a value in between 0.45 MPa (SL-2; CCs are detected) and 0.05 MPa (SL-1; CCs are not detected). If this strength difference is divided by the lithostatic pressure of the upper layer, we can generalize this statement to any problems involving a two-layer sharp model (strength ratio C; see Text S1 for more details). CCs can therefore form for impact velocity with U = 12.7 km/s if $\Delta C = \Delta Y_0/\rho g T > 0.03$–$0.27$, where ρ is the density of the upper layer and g is the gravitational acceleration.
2. The larger the difference in absolute strength between the two layers, the larger is the range of D_{RIM}/T at which CCs form (compare cases SL-4 and SL-6–SL-8). The transition from normal to concentric morphology occurs at a range between D_{RIM}/T = 5–11 (possibly even larger under extreme conditions, case SE-1). This is a much wider range than inferred from previous laboratory experiments (Q&O).
3. The transitions to concentric geometry (NC/CC or FBC/CC) happen at a rather specific D_{RIM}/T of 6.20 ± 0.29 for a given lower layer strength (SL-3, SL-5, SU-6, IV-1–IV-3, and PU-1–PU-3), which suggests that this transition is relatively independent of the properties of the upper layer, at least for a fixed impact velocity U = 12.7 km/s. There are exceptions such as cases SU-1 and SU-3, in which substantial collapse occurs in the upper layer (see section 3.3).
4. The transition from CC/NC at the high end of D_{RIM}/T is influenced by the properties of the upper layer and depends on the cratering efficiency of the layer (i.e., how much energy is consumed by crater formation in the upper layer and how much energy is transmitted into the substrate below). This is well illustrated by the decrease of the transition diameter with increasing strength (case SU-2) or the porosity (cases PU-2 and PU-3) in the upper layer as both leads to a reduction of the cratering efficiency.

3.2. FBCs

Most of our initial runs in Table 1 and Figure 6 included targets with strength contrasts <200 ($\Delta Y_0 \leq 4.95$ MPa and $\Delta C \leq 2.96$) at the average-impact velocity on the Moon U = 12.7 km/s. In those cases, crater morphology

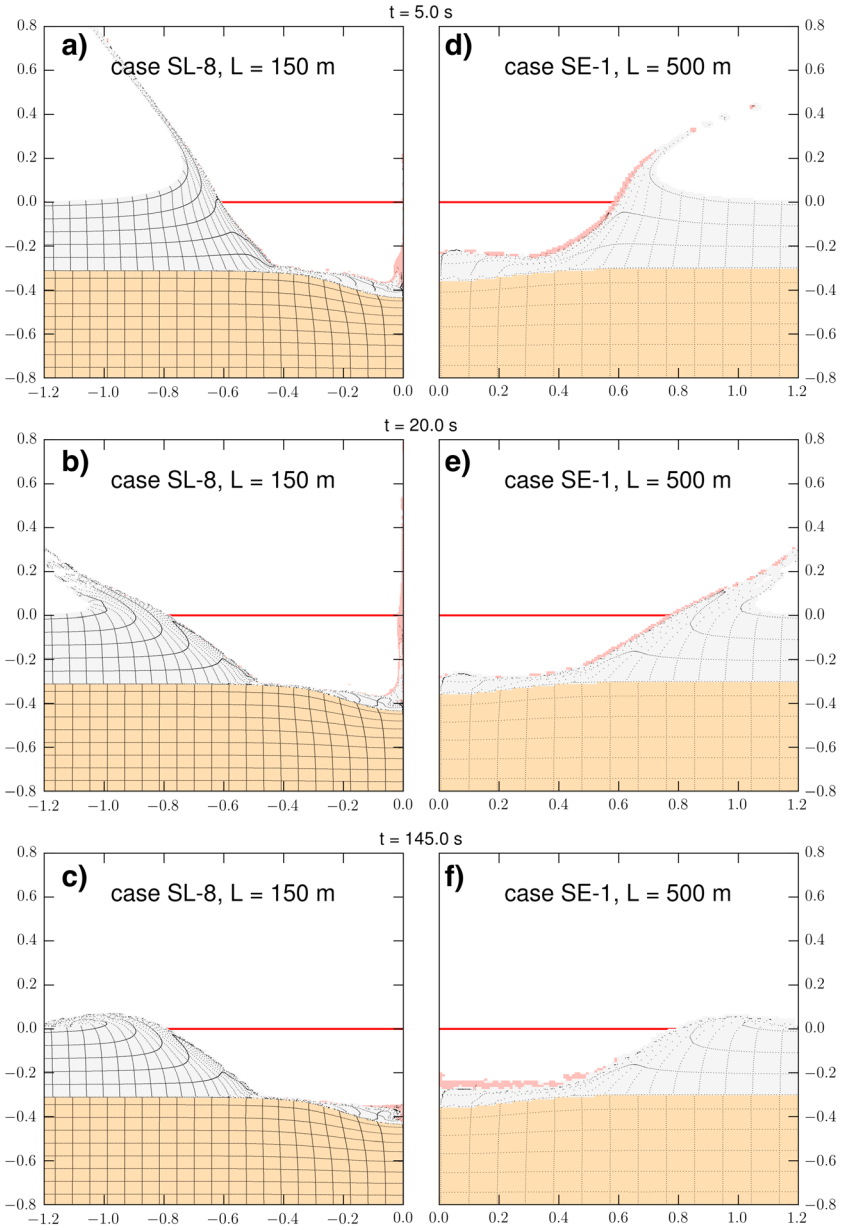

Figure 7. (a–c) Formation of a flat-bottomed crater in case SL-8, U = 12.7 km/s, L = 150 m, Y_0 = 0.1, and 100 MPa, for the upper and lower layers, respectively, f = 0.6 in the upper layer and Φ = 10%, which results in D_{RIM}/T = 6.4. (d–f) For case SE-1, which has the same properties as SL-8 but lower impact velocity (U = 1.0 km/s), L = 500 m, and results in D_{RIM}/T = 6.6. Other details are defined as in previous figures.

transitions directly from normal to concentric as the crater diameter increases. This behavior is somewhat different from laboratory-scale results that indicate a progressive NC/FBC/CC transition of crater morphology (Q&O). To investigate this discrepancy, we study cases with greater strength contrasts (cases SL-6, SL-7, and SL-8 by increasing the lower layer strength. This ultimately results in FBCs. The range of D_{RIM}/T ratios for which FBCs can form is broadened, owing to the increases in strength of the lower layers (Figure 6). We can reproduce the onset of the transition from NC to FBC (D_{RIM}/T = 4.2–4.3; Q&O), but the transition is limited to a smaller range of D_{RIM}/T = 4.0–6.5, compared to ~4.0–9.0 at laboratory scale. To test whether impact velocity plays a significant role, we reduce U to 1.0 km/s (case SE-1) using the target setup with the largest strength contrast (SL-8). With lower U, FBCs form over a wider range (D_{RIM}/T = 4.3–15.8), which indicates that impact velocity may have a relevant influence on the final crater morphology.

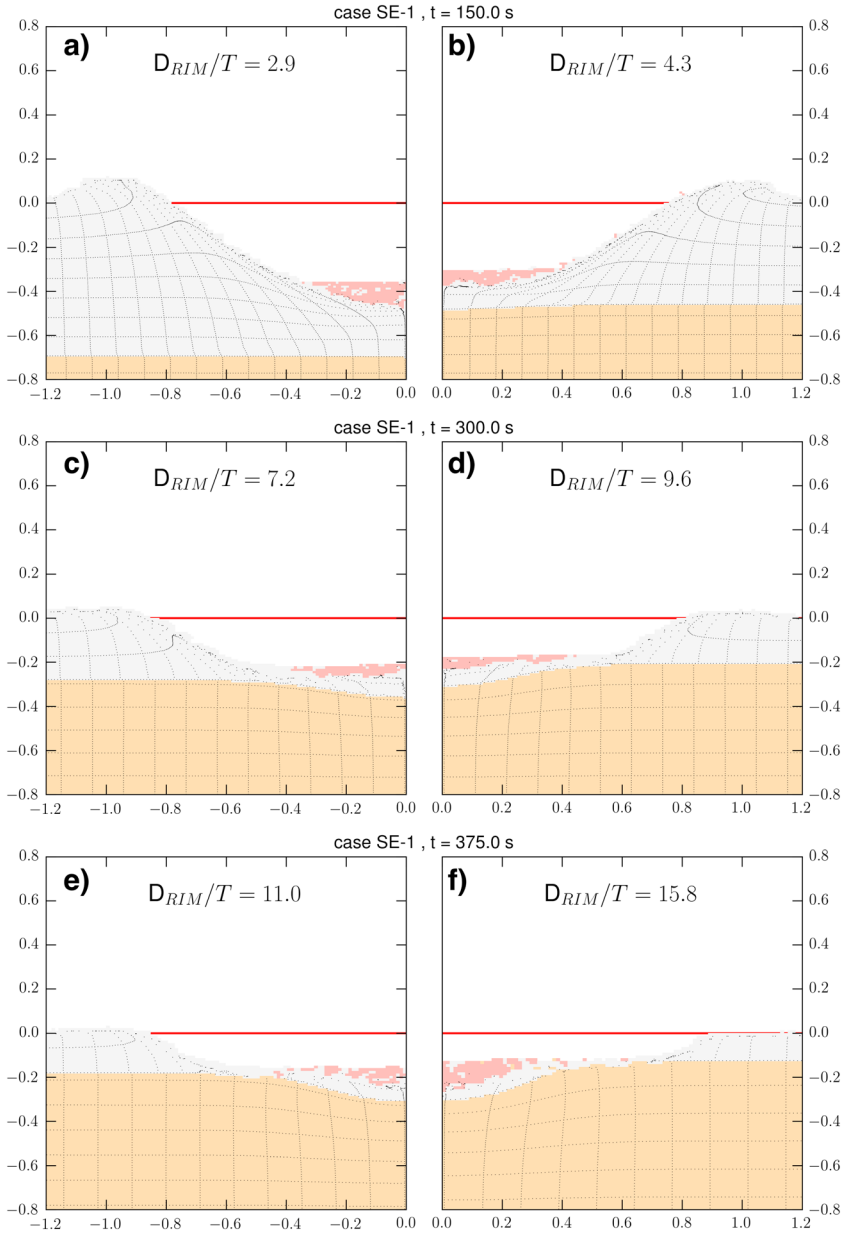

Figure 8. Final crater shapes for asteroid impacts with varying projectile diameters: (a) L = 200, (b) 300, (c) 600, (d) 800, (e) 1,000, and (f) 1,600. For all cases U = 1.0 km/s, f = 0.6, and Φ = 10%, Y_0 = 0.1 MPa (upper) and Y_0 = 100.0 MPa (lower), case SE-1. The ratio of the rim-to-rim diameter and the thickness of the upper layer (D_{RIM}/T) are specified in each subfigure. Other figure details are as in Figure 5.

Figure 7 depicts the final crater morphology for cases SL-8 and SE-1 for two different combinations of projectile diameters and impact velocities, which both result in similar $D_{RIM}/T \sim 6.5$. In both cases, FBCs form when the strength of the lower layer is large enough so that the upper layer deformation appears to decouple from the lower layer. This process is promoted by the low material strength of the upper and the large strength of the lower layer, which hinders material excavation. By employing larger and larger projectile energies (Figure 8, case SE-1), the diameter of the flattened crater floor increases and the impact energy transmitted to the target becomes at some point large enough to initiate cratering in the lower layer, apparently forming CC features (Figures 8e and 8f). However, the inner cavity is subsequently filled with collapsing material from the upper layer, which still leads to a flat-bottomed final crater. The formation mechanism of FBCs in our numerical simulations seems to be in general agreement with the formation of FBCs at laboratory scale (Q&O).

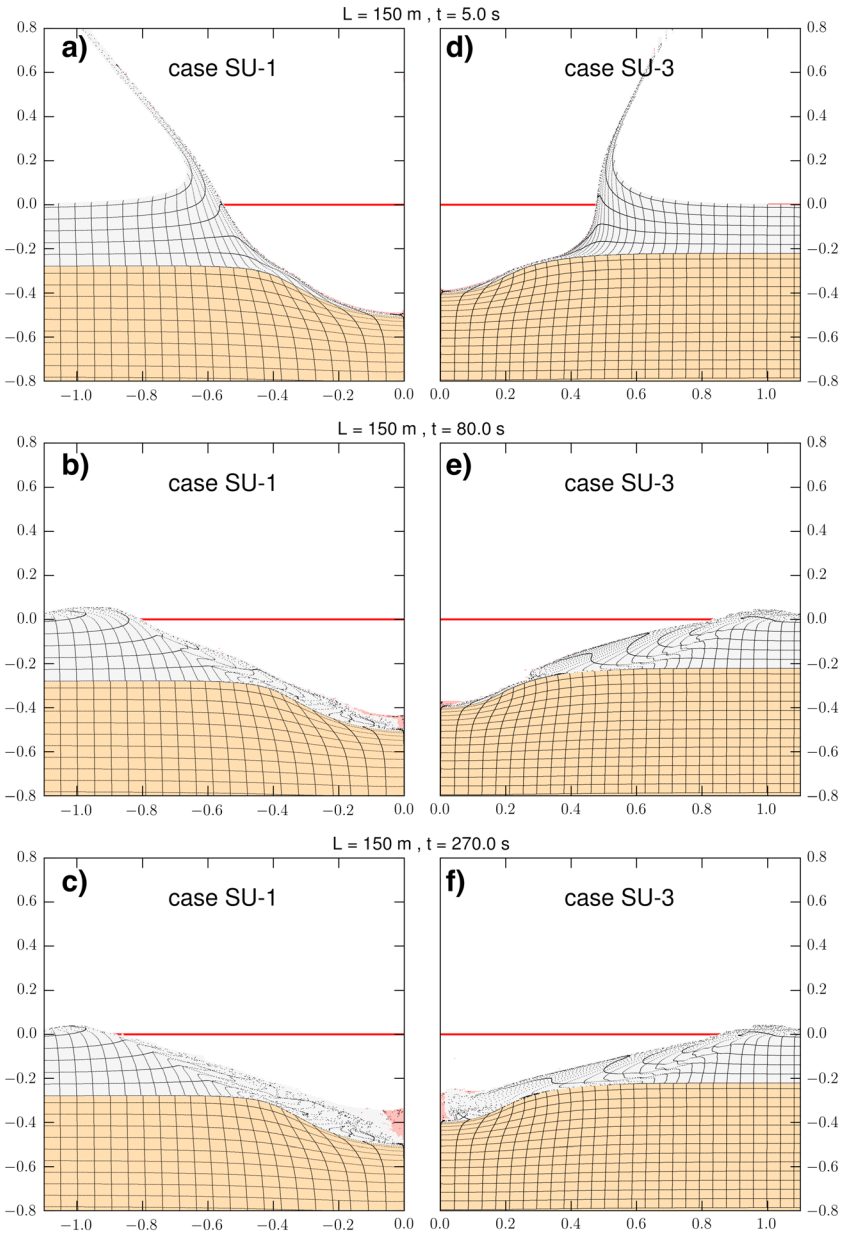

Figure 9. (a–c) Final crater shapes for case SU-1, U = 12.7 km/s, L = 150 m, Y_0 = 0.0, and 1.0 MPa, for the upper and lower layers, respectively, f = 0.6 in the upper layer and Φ = 10%, which results in D_{RIM}/T = 7.2. (d–f) For case SU-3, U = 12.7 km/s, L = 150 m, Y_0 = 0.1, and 1.0 MPa, for the upper and lower layers, respectively, f = 0.2 in the upper layer and Φ = 10%, which results in D_{RIM}/T = 9.0. Other figure details are as in Figure 4.

3.3. CMC

Figure 9 depicts the crater evolution of two cases (SU-1 and SU-3) that result in CMCs. In both cases, the upper layer decouples from the lower layer. However, because of the lack of cohesion (SU-1) and the low coefficient of friction (SU-3), a large amount of upper layer material collapses into the inner cavity. This strong collapse erases any indications of the concentric morphology and leads to the formation of a central mound in the center of the inner cavity (Figure 9c/9f). In most cases central mounds form only at an intermediate stage and flatten out as the modification process continues (see section 5.1).

Most of the collapsing materials fill the small inner cavities formed in the lower layer (Figures 10a–10c). Thus, although CCs are formed, the subsequent collapse erases any indication of it. This process seems to shift the transition from NCs to CCs to greater D_{RIM}/T ratios (= 9 and 11 for SU-1 and SU-3, respectively; Figure 6). We

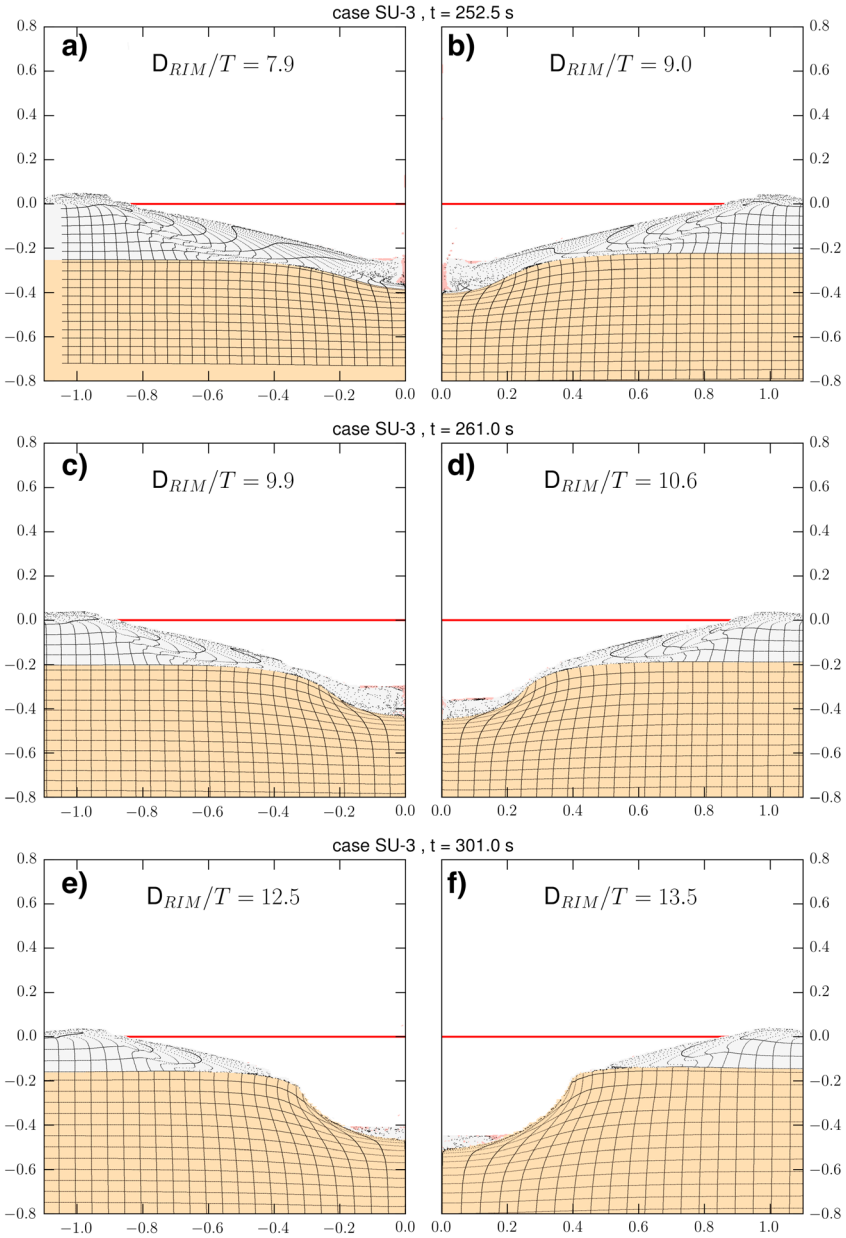

Figure 10. Final crater shapes for varying projectile diameters: (a) L = 120, (b) 150, (c) 180, (d) 200, (e) 250, and (f) 300. For all cases U = 12.7 km/s and Φ = 10% in both target layers, which have Y_0 = 0.1 MPa and f = 0.2 (upper) and Y_0 = 1.0 MPa and f = 0.6 (lower), respectively (case SU-3). The ratio of the rim-to-rim diameter and the thickness of the upper layer (D_{RIM}/T) are specified in each subfigure. Other figure details are as in Figure 5.

emphasize that these values are much greater than those obtained with little collapse in the upper layer (D_{RIM}/T = 5–6.5; section 3.1); consequently, the amount of collapse seems to play an important role in the variation of crater morphology as a function of crater diameter. With larger projectile diameter, impact energy increases and the upper layer decoupled more from the lower layer (Figures 10d–10f), and ultimately, the slope of cavity wall reaches the angle of repose of the upper layer material before the material completely fills up the inner cavity (Figures 10d–10f).

4. Comparison With Observations

The most visible morphological features for relatively small craters ($D_{RIM} < 400$ m) are the inner (D_I) and the rim-to-rim crater diameter (D_{RIM}) of CCs. Both are relatively easy to measure on the Moon via remote sensing

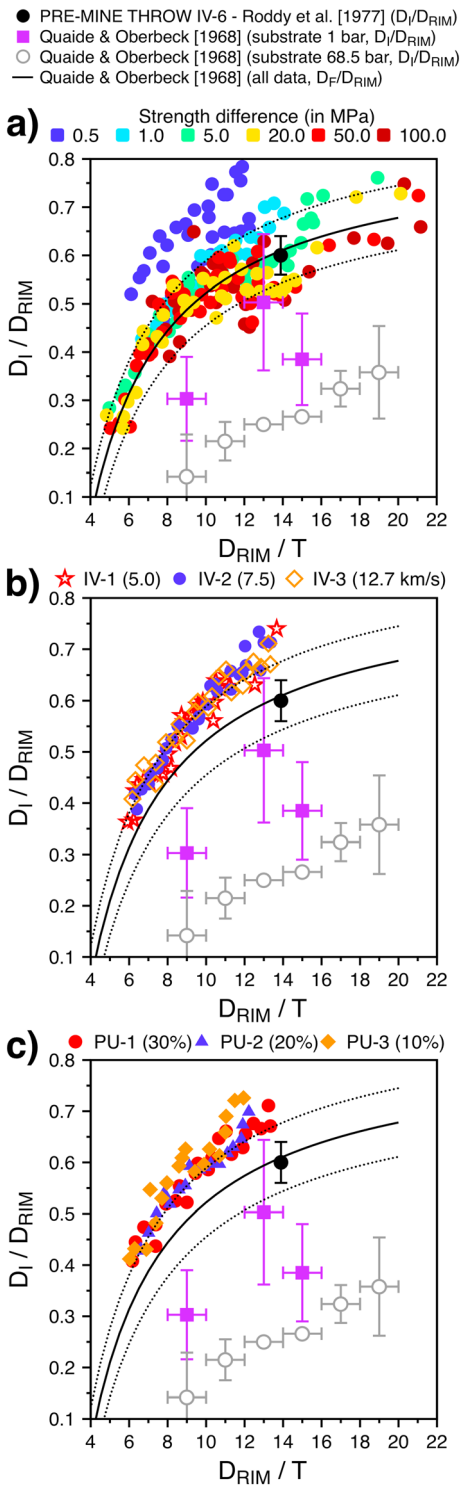

Figure 11. Ratios of inner craters and rim-to-rim crater diameters (D_I/D_{RIM}) as a function of the relative thickness D_{RIM}/T for projectile diameters L = 70–1,500 m (resulting in CCs) and for (a) different strength differences (cases with change in coefficients of friction not included here), (b) impact velocity, and (c) upper layer porosity. Results are compared at the top of the figure to laboratory-scale experiments conducted in Q&O and a terrestrial CC produced during PRE-MINE THROW IV-6 crater explosion (Roddy, 1977). Uncertainties are taken from literature when available.

images and thus provide observables to compare our modeling results to. First, we evaluate how well our model craters replicate the morphology of CCs at laboratory scale (Q&O). Figure 11 depicts the ratio between the inner and rim-to-rim crater diameters as a function of the relative thickness D_{RIM}/T. For a given D_{RIM}/T, a large D_I/D_{RIM} ratio indicates weak decoupling, whereas small D_I/D_{RIM} indicates strong decoupling. The smallest decoupling is obtained for strength- over strength-dominated cases and gravity- over strength-dominated cases, more particularly in cases where some of the initial impactor energy dissipates through the compaction of pores (porosity dependent; PU-2 and PU-3; Figure 11c) or in cases with large upper layer strength, where the energy is consumed through material's deformation (strength dependent; SU-2, strength difference = 0.50 MPa; Figure 11a). On the other hand, the greatest decoupling is observed for impacts into targets with greatest differences in strength (Figure 11a).

More generally, D_I/D_{RIM} *increases* with D_{RIM}/T from about 0.3 to 0.8. While some variations due to different target properties are observed, we find no clear dependency on the impact velocity between U = 5.0–12.7 km/s (Figure 11b). Compared to Q&O's work, our results typically show greater D_I/D_{RIM}, which may indicate that the decoupling between upper and lower layer is more pronounced at laboratory scale. In the laboratory experiments the ledges may be twice as wide as the inner crater itself (e.g., Figure 12 in Q&O), while in most of our numerical models, the crater floor diameters D_F are about the same size as the inner crater diameters (Figures 3 and 12). This could relate to the large material strength used at laboratory scale (see Text S1 and Table S2). As we increase the strength contrast in our models (cases SL-6, SL-7, and SL-8), the decoupling increases and so does the differences between D_F and D_I (see definitions in section 2.3 and Figure 2). This explains well why our relations for D_I/D_{RIM} differ from Quaide and Oberbeck's D_F/D_{RIM} for large strength contrasts and get closer to D_{IL}/D_{RIM} for the lowest substrate strength.

We also compare our modeling results to observations on the lunar surface, specifically in three lunar maria (Mare Crisium, Mare Tranquillitatis, and Oceanus Procellarum). Figure 12 shows examples of six lunar CCs on Mare Crisium. From the shadow casts no clear decoupling of the upper and lower layer becomes evident. The ledges are rarely flat and their lengths are often smaller than 0.1 D_{RIM} (Figure 12c/12d/12f). Typically, the inner crater rim exhibits an irregular shape (Figure 12e) and central mounds are centered within the inner crater (Figures 12c–12f).

For a more quantitative analysis, we measure the relation between D_I and D_{RIM} for about 100 CCs in each of the three maria and compare their distribution of D_I/D_{RIM} (Figure 13). Generally, the diameter range-over which CCs are observed is similar for the three maria (Figure 13a) and all regions feature a similar distribution of magnitude of layer decoupling (Figures 13b and 13c). In Oceanus Procellarum, however, the transition back to NC morphology occurs at D_{RIM} ~ 150 m compared ~200 m observed for the two other regions (Figure 13a). A smaller transition diameter may point to a thinner regolith layer and a younger resurfacing age in Oceanus Procellarum (Bart et al., 2011; Oberbeck & Quaide, 1968). Since the uncertainties in our D_{RIM} and D_I

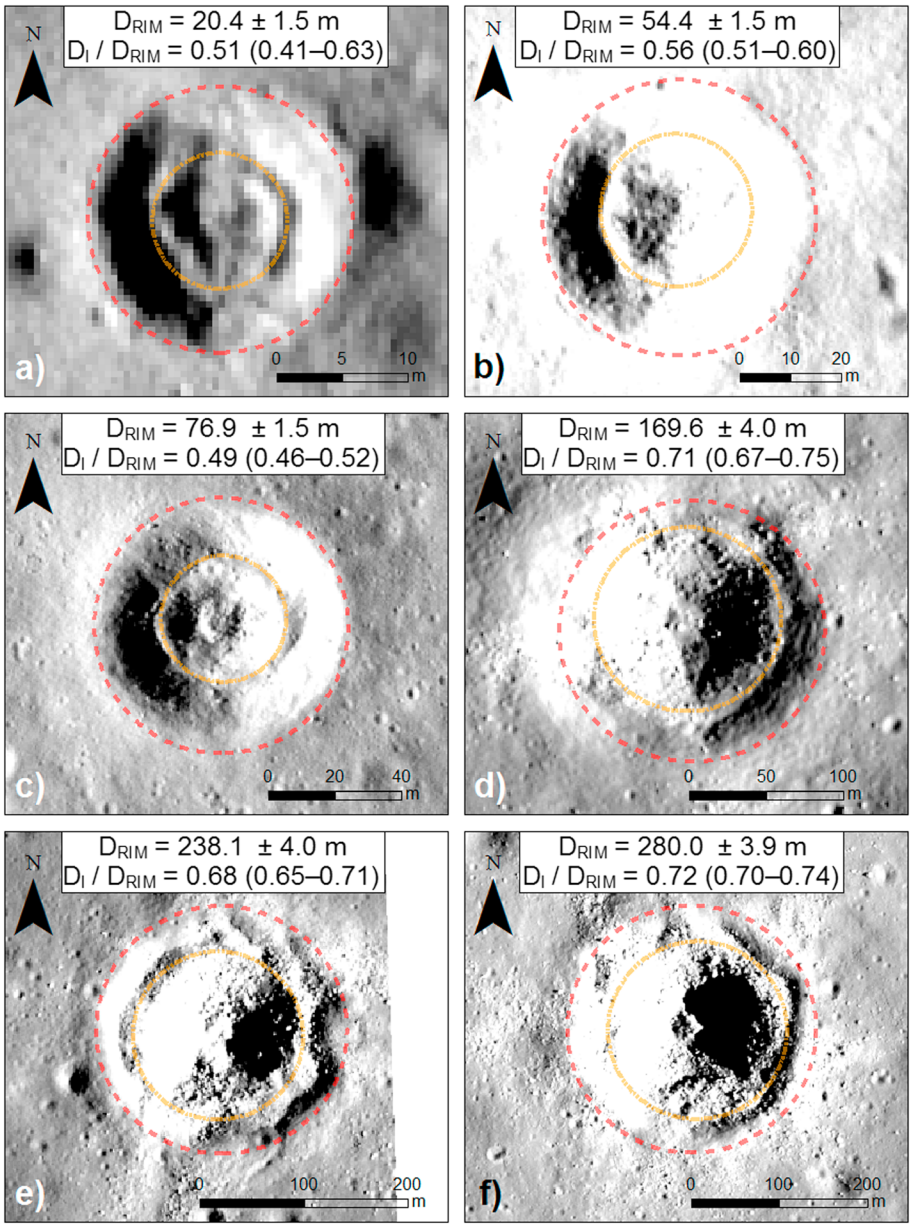

Figure 12. Six lunar concentric craters (from NAC images: M134808666LE, M134808666RE, M192567794LE, and M1107881882RE) observed on Mare Crisium. In all cases, the inner-crater diameter (D_I; orange dash-dotted line) and the rim-to-rim crater diameter (D_{RIM}; red dashed line) are measured. Their ratio and D_{RIM} are specified at the top of each subfigure. Values in parentheses depict the maximum variation in D_I/D_{RIM} based on the ±3 pixel resolution uncertainties in the location of D_I and D_{RIM}.

determination is largest at small crater diameter (due to limited image resolution), we tested whether the distribution of observed D_I/D_{RIM} is biased by the small craters. We excluded craters with rim-to-rim diameters $<$50 m, but observed no significant changes (Figure 13c). The distribution of the observed ratios seems fairly robust and matches our numerically inferred ratios.

So far we only discussed the lateral crater dimensions, but now we investigate also the vertical dimensions, that is, crater depth and the height of ledges above the crater floor. We compare the topographic cross section of one fresh lunar CC with D_{RIM} = 185 m on Mare Crisium and of one terrestrial CC formed by a large explosion experiment (PRE-MINE THROW-IV 6; Roddy, 1977) with two of our model cases. We use model case SL-7 with little collapse and model case SU-3 with strong collapse in the upper layer (Figure 14). The

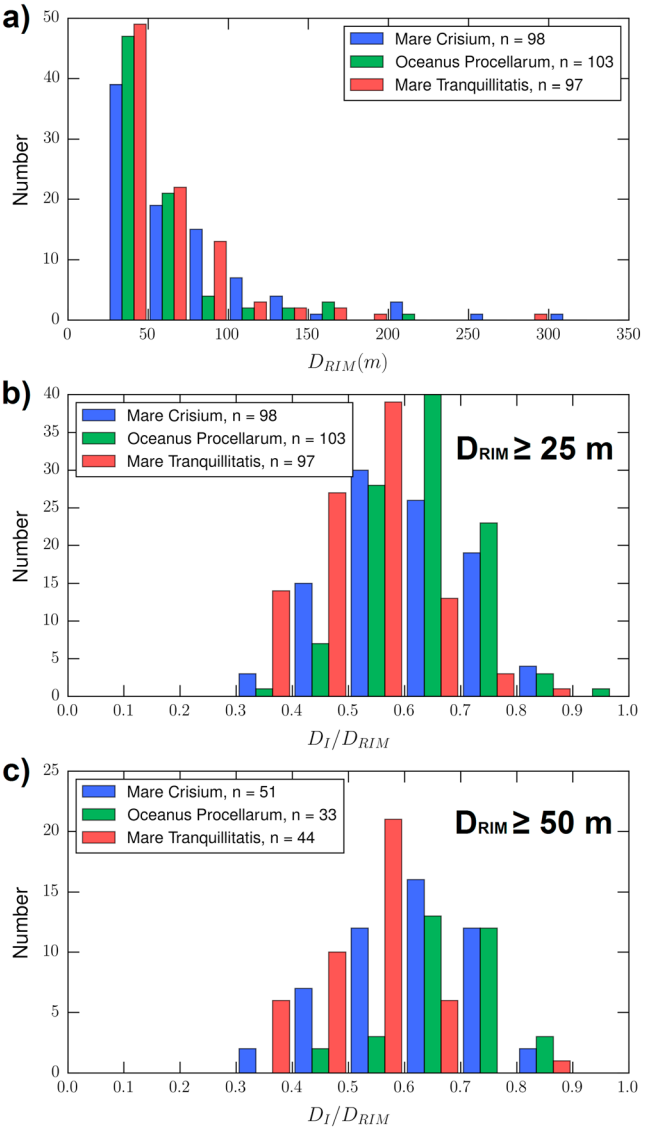

Figure 13. (a) Number of concentric craters within a rim-to-rim crater diameter range (bin size = 25 m). Distributions of ratios of inner to rim-to-rim crater diameters (D_I/D_{RIM}) for Mare Crisium, Mare Tranquillitatis, and Oceanus Procellarum for (b) $D_{RIM} \geq 25$ m and (c) $D_{RIM} \geq 50$ m. The bin size of the histograms is equal to 0.1.

numerical simulations consistently result in deeper craters with much greater d_r/D_{RIM} = 0.19–0.23 (where d_r is the maximum depth from the rim crest). In contrast, most of fresh craters on the lunar surface with $D_{RIM} < 400$ m feature d_r/D_{RIM} = 0.12–0.20 (Basilevsky et al., 2014; Daubar et al., 2014; Mahanti et al., 2017; Stopar et al., 2017), while the fresh lunar CC on Mare Crisium has d_r/D_{RIM} = 0.09–0.11 (Figure 14). This could be attributed to the fact that we employ changes in target properties at sharp interfaces rather than gradual transitions. Also, we omitted the effect of dilatancy in our numerical setup, which results in a limited collapse of the upper layer. Dilatancy affects materials that undergo shear deformation (Collins, 2014), and as our lower layer is stronger than the upper layer, we expect dilatancy to be mostly relevant in the upper layer. For CC formation, dilatancy may therefore be more likely to affect the slumping of the upper layer down the cavity wall (influencing the rim-to-rim crater diameter) rather than the inner crater rim D_I. As long as this assumption is valid, our results will be similar for numerical models with and without dilatancy. We emphasize, however, that results need to be interpreted with caution for transitional crater morphologies (i.e., close to transitions between NC/FB/CC) as a dilatancy-enhanced collapse of the upper layer could influence transitions from a crater morphology to another. Based on the comparison of numerical study employing a Drucker-Prager strength model and laboratory experiments (Collins et al., 2011), numerical simulations including dilatancy (Collins, 2014), crater collapse at laboratory scale (Yamamoto et al., 2006), and geophysical observations at simple terrestrial impact structures (Grieve & Garvin, 1984), we expect our modeled crater depths to be overestimated by ~20% and modeled rim-to-rim crater diameters to be underestimated by ~5–10%. As a consequence, our calculations for D_{RIM}/T may also be underestimated by the same ~5–10% and D_I/D_{RIM} overestimated by ~5–10%. Future investigation is required to exactly determine how crater formation in layered targets is influenced by dilatancy model parameters. Lowering the coefficient of friction tends to significantly increase the amount of collapse during crater formation, which possibly mimics the expected effect of dilatancy to some extend (see section 2.1). However, even with very small coefficients of friction (SU-3, f = 0.2), our model still does not reproduce the topography (and the depth-diameter ratio) of the fresh lunar CC very well. Another explanation could be related to the large impact velocity and the simplified strength model used in our numerical study. Indeed, a recent study on secondary craters on Mars (Watters et al., 2017) has shown that a more sophisticated strength model (Collins et al., 2004) coupled with dilatancy (Collins, 2014) and low-impact velocities U = 0.2–2 km/s results in d_r/D_{RIM} from 0.09 (U = 0.2 km/s) to 0.20 (U = 2.0 km/s). Finally, fast postmodification processes of craters such as mass wasting and seismic activity could also influence crater morphology significantly (Basilevsky et al., 2014; Richardson et al., 2004, 2005; Xiao et al., 2013).

Compared to the terrestrial example, the numerical models match rather well with the cross section of PREMINE-THROW IV 100-ton crater 6. Although the strength discontinuity is not located at the same normalized depth, both the normalized maximum depth (<10% difference) and the ledge's lengths seem to match relatively well. This better agreement is likely an indication of a crater formation process that was limited by the material strength of the target, which results in deeper craters with greater depth-diameter ratios, similar to our numerical results.

Despite the number of simplifications and limitations involved, we point out that all crater morphologies observed on the lunar surface for $D_{RIM} < 400$ m are successfully reproduced with the help of our simple

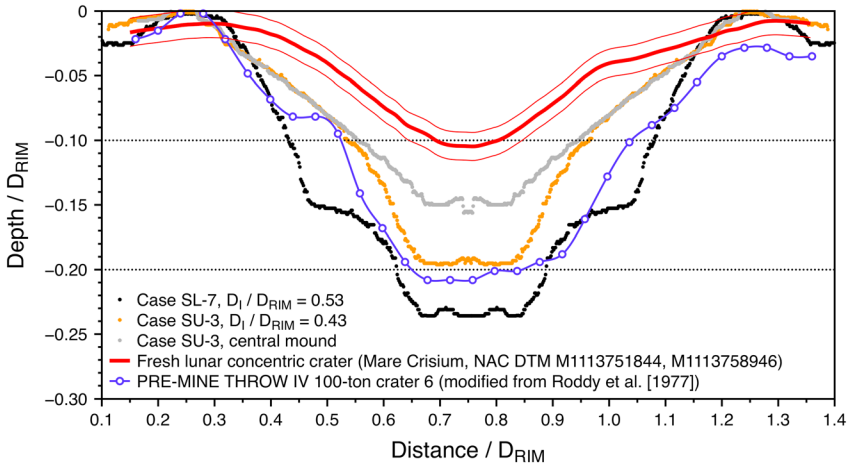

Figure 14. Elevation profiles of a lunar concentric crater on Mare Crisium (from NAC images: M1113751844 and M1113758946), a terrestrial concentric crater (PRE-MINE THROW IV crater 6; Roddy, 1977), and cases SL-7 and SU-3. All of these profiles have an inner to rim-to-rim crater diameter ratio ~0.5. Distance and depth values are normalized with the rim-to-rim crater diameter of each of those craters. The elevation profile for the lunar concentric crater is extracted from product NAC_DTM_M1113751844_M1113758946 created by ASU LROC teams with the NASA Stereo Pipeline (ASP) from pairs of NAC images (Brown et al., 2017). The thin red lines depict a ±1 m uncertainty in elevation.

model. The formation of CCs with respect to final crater diameters seems to be in accordance with observations of small lunar CCs (Figures 7, 13, and 14). The observed magnitude of the decoupling for lunar CCs was captured by the range of target properties studied (Figures 12–15). We were able to reconstruct more complex interior morphologies at greater D_{RIM}/T in our numerical models, as, for example, the morphologies shown in Figure 12c/12e for lunar CCs are recovered in models such as SL-5 (Figures 5e–5g).

5. Discussion

5.1. The Role of Impactor and Target Properties in the Formation of Simple Crater Morphologies

We performed numerical model simulations that cover a large range of target properties compatible under lunar conditions. We demonstrated how simple crater morphology may vary across the lunar surface as a function of these properties. A key finding of our work is that crater morphology does not necessarily follow a typical sequence—from NC to FBC to CC (back to normal)—when projectile diameter increases for a given subsurface discontinuity as suggested by the laboratory experiments of Q&O. Indeed, the conditions under which CC and FBC are formed in a layered target depend on several factors, in particular, (1) the thickness of the upper layer, (2) the absolute strength of the upper and lower layers, (3) the coefficient of friction of the top layer, (4) how much initial impact energy is transmitted to the substrate, and (5) the impactor velocity. The factors (2–4) are all dependent on target properties, which thus play a first-order role for the morphology of simple craters formed in near-surface stratigraphy.

More specifically, CCs form if (1) the difference in strength between layers is large enough (in agreement with simulations made by Senft & Stewart, 2007), (2) the relative thickness (D_{RIM}/T) is within a specific range (which depends on target properties and impact velocity), and (3) the strength of the upper layer is smaller than the lower layer. CCs form regardless of whether crater evolution in the upper layer is controlled by target strength or by the target's gravity (cases SU-1 and SL-5, Figures 3d–3f and 4d–4f, and SU-2). CCs may form at very low layer strength contrast (factor of 2; e.g., case SU-2) as it has been suggested by Wilcox et al. (2005) and has been observed in situ at several Apollo landing sites (Muehlberger et al., 1972, 1973; Schmitt, 1973; Shoemaker et al., 1970; Swann et al., 1972). Thus, CCs do not necessarily form due to the interface between lunar regolith and mare basalt but may also develop in a target with multiple basaltic or regolith layers with slightly different strengths (e.g., CCs with multiple inner craters; Figure 20 in Q&O; Wilcox et al., 2005).

The formation of CCs in targets with multiple strength layers may also be in line with the presence of lunar CCs with $D_{RIM} > 1$ km, such as the one observed on the smooth floor of Humboldt crater

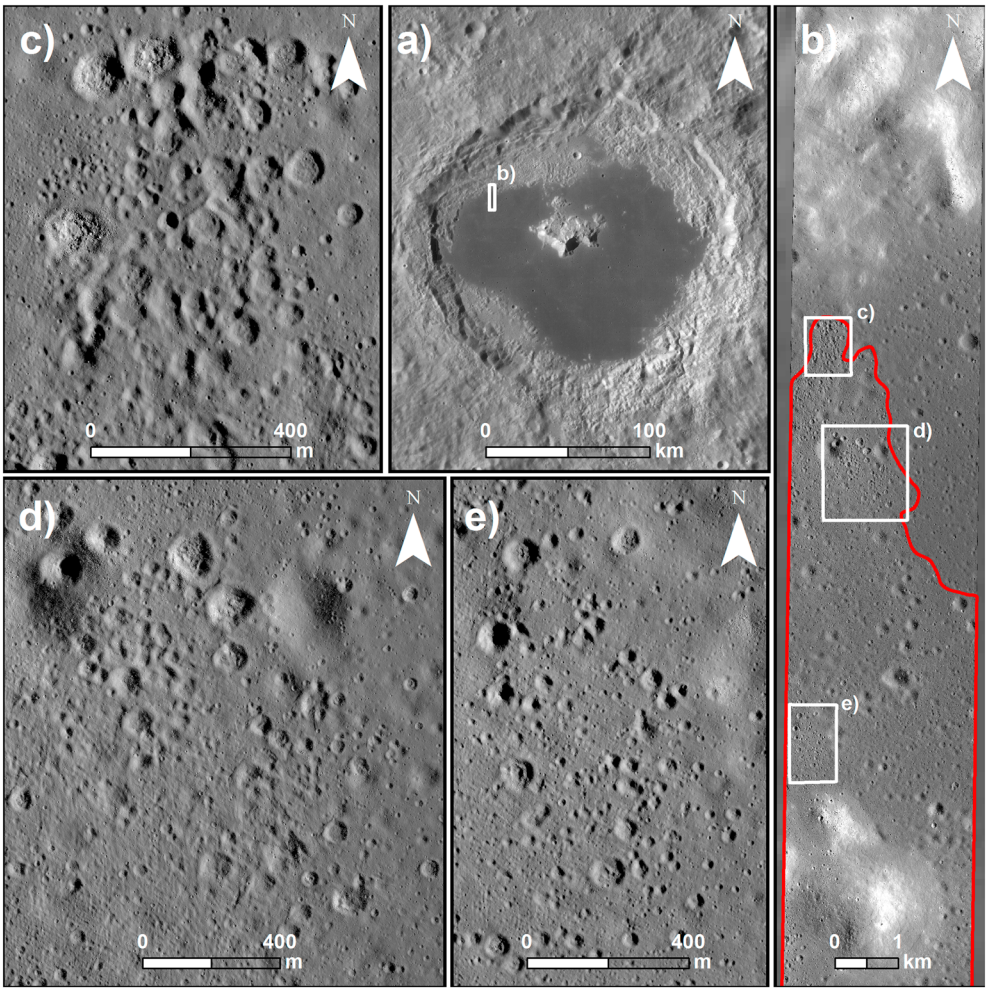

Figure 15. (a) Tsiolkovskiy crater on the farside of the Moon (WAC morphology basemap [NASA/GSFC/Arizona State University]). (b–e) Several locations on the floor of Tsiolkovskiy crater (NAC image M161475783R [NASA/GSFC/Arizona State University]) where clusters of secondary craters are visible. The area with higher crater density is outlined by a red line in panel (b). Panels (c)–(e) show a large number of FBCs, which may be caused by low-impact velocity and the presence of a strength discontinuity at depth.

(D_{RIM} = 207 km; Wood, 1978). These large CCs likely originate from a strength discontinuity, possibly caused by impact melt overlying an originally deep-seated stronger material. CCs with $D_{RIM} < 400$ m form only on the lunar maria, whereas they are largely absent on the rougher, older lunar highlands (Q&O). Therefore, not any strength discontinuity is sufficient to produce the different crater morphologies as suggested by Wilcox et al. (2005).

However, a CC will only form if $\Delta C = \Delta Y_0/\rho g T > 0.03$–$0.27$ (strength difference between layers normalized to the lithostatic pressure of the upper layer) for U = 12.7 km/s and if the collapse does not erase any morphological evidence of the strength discontinuity (Figures 3d–3f and 4). This statement is valid independent of the magnitude of the strength contrast. If these conditions are not satisfied, a decoupling will not happen (e.g., case GG-1 in Figures 4a–4c and case SU-1 and SU-3 in Figures 9/10a and 10b). Such conditions may be relevant to explain the almost absence of CCs on the lunar highlands. As the highland's surface is older, the regolith layer is likely thicker (Oberbeck & Quaide, 1968). If CCs existed on the lunar highlands, they would (1) have greater rim-to-rim crater diameters than their counterparts on the lunar maria and (2) require stronger lower layer (s) due to the larger lithostatic pressure. The stronger bombardment on the older highland may have led to a higher weakening of the near-surface layers and to a more gradual change in target properties, so that the difference in strength between individual layers may be insufficient.

The possibility to form CCs for low strength contrast has implications for the estimation of lunar regolith thickness from observed crater morphologies (e.g., Fa et al., 2014, Oberbeck & Quaide, 1967, 1968, Quaide & Oberbeck, 1968). The presence of a slightly more resistant layer within the regolith may be sufficient to allow for CC formation even at smaller rim-to-rim diameters reaching less deep into the target, which would then decrease the estimate of regolith thickness (*Fa* et al., 2014). Consequently, regolith thickness estimates inferred from crater morphologies may be considered as a lower limit since the unconsolidated-substrate layer does not necessarily coincide with the real interface between regolith and mare. In these estimates, the term regolith thickness should practically be redefined as the depth of the first strength discontinuity, which may or not be the regolith-mare interface.

Finally, we emphasize that our criterion $\Delta C > 0.03$–0.27 seems to identify the conditions suitable for CC formation rather reliably. For example, at laboratory scale, the uppermost layer is often represented by a few centimeters of sand (such as $T \sim 10$ cm, $g = 9.81$ m/s^2, and $\rho = 1{,}600$ kg/m^3). If we apply this target condition, assume an impact velocity of 12.7 km/s, a $\Delta C > 0.03$–0.27, and use the equation S2 in the supporting information, a difference in cohesion of $\Delta Y_0 > 47$–424 Pa is calculated. Such findings would explain why CCs do form in laboratory impact experiments involving multilayered targets with small strength differences such as colored over plain sands and loose over dense sands (Piekutowski, 1977; Stöffler et al., 1975).

In contrast to CCs, FBCs form only for specific combinations of material strengths and impact velocities, which indicates the significant effect of these parameters on the variation of crater morphology with increasing crater diameter. Our results suggest that FBC formation likely happens below a threshold impact velocity U_{min}, which depends mostly on the lower layer material strength. This conclusion is drawn from three important observations. First, in the first set of numerical cases (SL-family), no FBCs formed for large impact velocity $U = 12.7$ km/s and moderate strength contrast (< 200). The impact-induced energy reaching into the lower layer was always large enough to overcome the strength of the layer and thus its resistance to deformation. This initiated cratering, such that crater morphology transitioned directly from NCs to CCs without an intermediate FBC stage. Consequently, the impact velocity, which determines the impact-induced energy for a given projectile mass, was supercritical ($U > U_{min}$). Upon increase of the lower layer strength (cases SL-5–SL-8), more and more energy is required to initiate cratering in the lower layer, so that the impact velocity becomes subcritical at some point ($U < U_{min}$) and FBCs eventually start to form. Consequently, for very low-impact velocities—such as for secondary impacts that impact at velocities smaller than the lunar escape velocity of $U < 2.38$ km/s—the available energy for deformation in the lower layer is very small and FBCs may form also at reduced lower layer strength. Moreover, the formation of FBCs at very low U occurs over a much greater range of crater diameters, which is well reflected by case SE-1 ($U = 1.0$ km/s) in which the transition diameter to concentric morphology is increased by more than a factor of 2 compared to the respective case with high-impact velocity (see Figure 6).

Conceptually, crater morphology variations are well illustrated by two end-members: an infinitely strong lower layer or an infinitely large impact velocity. In the first case, for any impact velocity, the pressure generated in the target will be insufficient, that is, $U \ll U_{min}$, and NCs transition to FBCs, but will never transition to CCs. In the second case, for an infinitely large impact velocity, the pressure generated will be always much larger than the strength of the lower layers, so that $U \gg U_{min}$. Therefore, crater morphologies will transition directly to CCs. Q&O investigated the effect of impact velocity for $U \leq 7$ km/s. However, no clear influence on crater morphologies was observed. Here we speculate that the lower layer strengths used in the experimental setup of Q&O was very large for laboratory-scale impact experiments (see Text S2). This seems to be in agreement with the ledge lengths of the laboratory CCs being much greater than the ones of lunar CCs (Figures 12 and 13). Based on cases SL-8 ($U = 12.7$ km/s) and SE-1 ($U = 1.0$ km/s), which are the most similar cases to these laboratory experiments, we speculate that $U_{min} > 7$ km/s so that no clear shift in the transition diameter from FBCs to CCs could have been observed at Q&O's laboratory scale experiments.

Given the above discussion about the formation of FBCs, we expect that a population of FBCs with significantly different diameters may indicate low-impact velocity and thus possibly secondary impacts. However, we emphasize that smaller strength discontinuity in the target could generate FBC or CC morphologies at low-impact velocity, but not at sufficiently large impact velocity (i.e., the value of ΔC depends on impact velocity). Since the impact velocity for individual impacts is typically unknown, the absence of FBCs

and CCs does not necessarily indicate the absence of one or more strength discontinuities or a gradual change in the shallow target structure.

Finally, we discuss the CMC morphology, although it occurs in only a few of our models (e.g., Figures 10 and 11), while it appears more frequent within observed normal and concentric lunar craters, regardless of their size (Figures 13c–13f). We observe CMC formation when a gravity-dominated upper layer overlays a strength-dominated lower layer, but only if the upper layer strength is low enough to allow for material slumping down into the inner crater cavity (e.g., SU-1 and SU-3) or on the flattened crater floor (e.g., SE-1). The formation of CMC is thus partially different from what was observed in Q&O. At laboratory scale, CMCs are only an intermediate stage between NCs and FBCs originating from the slumping of upper layer material down onto the flattened crater floor at $D_{RIM}/T \sim 4$ and seem to happen only before material in the lower layer starts to be excavated. Our results suggest that the same process occurs also when a CC is formed and would therefore explain why numerous central mounds are also observed in the center of lunar CCs (Figure 12). Although CMCs are produced in our numerical models, we point out that they are often not stable and typically flatten out as the modification process goes on. Possibly, this relates to the Drucker-Prager material model, which describes the resistance of matter against deformation (strength) not sufficiently accurately. The absence of dilatancy in our models may also play a role here. Future work including dilatancy is required to study the formation of central mounds in detail. Another possibility could be that central mounds form not only during crater formation or crater collapse but also later due to seismic activity (Richardson et al., 2004, 2005) or other later mass-wasting processes on the lunar surface (e.g., Xiao et al., 2013). Such processes happen on much longer timescale and are therefore not captured by our models. Although central mounds are not always reproduced in our model, we do not expect this to have a large influence on the previous observations we made for FBC and CC.

5.2. Implications for Regolith Thicknesses Derived From Crater Morphologies

Our results suggest that deviations from normal simple bowl-shaped crater morphology (NC/FBC and NC/CC) happen somewhere between D_{RIM}/T = 4–11 and the transition to concentric geometries somewhere between D_{RIM}/T = 5–16 (NC/CC and FBC/CC), depending on both impact velocity and target properties. These wide ranges of values aggravate the estimation of regolith thickness from crater morphologies. If we use the transition at $D_{RIM}/T = 9$ for concentric geometries (Q&O), an actual transition at $D_{RIM}/T = 16$ (5) would result in a 44% decrease (*80% increase*) in the estimated regolith thickness. Likewise, assuming a $D_{RIM}/T = 4$ as the upper boundary for forming normal bowl-shaped craters (Q&O) would cause a 20–74% decrease in estimated regolith thickness from normal geometries.

Fa et al. (2014) characterized more than 350,000 craters across Sinus Iridum (D_{RIM} = 5–250 m) in terms of their morphologies. Three arguments in their study support a complex crater evolution of simple craters with crater diameters as reported here. The distributions of normal, flat-bottomed, and concentric geometries peak at the same crater diameter D_{RIM} = 15–20 m (Figure 9 in Fa et al., 2014). If FBCs were produced over smaller D_{RIM}/T = 4–9 than concentric geometries $D_{RIM}/T > 9$ (Q&O), we would expect them to be consistently produced at smaller crater diameters. However, this pattern should be recovered in the distribution of the crater morphologies, which is clearly not the case. The estimates of the regolith thickness made from NC/FBC are consistently greater (1–12%) than estimates made from FBC/CC. Finally, the regions covered by secondaries indicate a much greater variation in regolith thickness estimates between results inferred from the NC/FBC and FBC/CC transitions (22–49%). We suggest four alternative reasons for this discrepancy: (1) regolith thicknesses derived from NC geometries may be overestimated and the separation between normal and other crater morphologies may occur at greater D_{RIM}/T than previously thought; (2) the regolith thicknesses calculated from normal geometries are correct, so that the onset of transition to CC morphologies happens at lower D_{RIM}/T than previously thought; (3) because of the dependence on strength properties and impact velocity, neither of the two estimates are correct and shifts in the transition onset of both crater morphologies are possible causes; and (4) the strength discontinuity at the origin of transitions in crater morphologies does not always represent the regolith-mare interface, and would thus introduce a large variability in thickness estimates.

For secondary craters (at low-impact velocities), our model results suggest that most crater morphologies are more likely to go through a sequence NC/FBC/CC with increasing impactor energy. Observations of a large

number of FBCs within clusters of secondaries on the floor of Tsiolkovskiy support that low-impact velocities may facilitate the formation of this crater type (Figures 15a–15e). The transition from NC to FBC seems to be relatively unaffected by target properties and impact velocities and occurs at relatively constant $D_{RIM}/T = 4.25 \pm 0.05$ in our models (e.g., cases SL-6, SL-7, SL-8, and SE-1). The transition may therefore be used to estimate lunar regolith thickness more robustly. We point out that this relatively constant transition may be due to the relatively constant depth-diameter ratio (d_r/D_{RIM}) we observe in our models regardless of the impact velocity. In most cases, d_r/D_{RIM} is ~0.24, which corresponds well to the transition at $D_{RIM}/T = 4.25$ (1/4.25–0.24). However, fresh and small lunar craters ($D_{RIM} < 400$ m) rarely have depth-diameter ratios greater than 0.20 (Basilevsky et al., 2014; Daubar et al., 2014; Mahanti et al., 2017; Stopar et al., 2017). Moreover, Watters et al. (2017) suggest that the depth-diameter ratio of secondary craters on Mars might decrease significantly with decreasing impact velocity, from $U = 2$ km/s (~0.22) to $U = 0.2$ km/s (~0.09). The greater variability in depth-diameter ratios could therefore also influence when the transitions in crater morphologies occur. For $U = 0.2$ km/s and $d_r/D_{RIM} = 0.09$, the transition may be expected to occur for $D_{RIM}/T = 1/0.09 = 11.1$, which further aggravates the interpretation of crater morphologies. However, the transition from NC to FBC seems to be the most robust transition and should therefore be preferentially used. For future studies in which the number of FBCs may be limited, our model-derived, empirical relationship between D_{RIM}, D_l, and T (e.g., Figure 11) might provide another method to estimate the regolith thickness. For instance, if D_{RIM} and D_l are measured via remote sensing techniques, one can directly derive the uppermost layer thickness T. A better quantitative understanding of target properties and their regional variations is still essential to improve the robustness of the here presented relationships though. As the target properties of the lunar maria can vary considerably at regional scale (Kiefer et al., 2012; Wieczorek et al., 2013), more information on target properties at planetary-scale is essential and required for future improvements.

6. Conclusion

The purpose of the current study has been to constrain suitable conditions for the formation of the different crater morphologies of simple craters observed on the lunar surface (normal, central-mound, flat-bottomed, and concentric). These different morphologies result from variations in target properties and depend on impactor mass and velocity (Figure 16). Since these properties are typically unknown for natural, planetary impacts, the interpretation of the lunar cratering record with regard to the shallow lunar structure is complicated. To address these issues, we have used a numerical modeling approach and have investigated simple crater formation in a layered target with two horizontal layers. Our models reproduce crater morphologies consistent with lunar craters for rim-to-rim diameters of 400 m or less. From our modeling results, we draw the following conclusions:

1. CCs only occur if the difference in cohesion between strength layers (defined as ΔC, if normalized to the lithostatic pressure of the uppermost layer) is above a threshold value and if the collapse in the uppermost layer does not fill up the newly formed inner cavity. The ΔC depends on the strength difference between upper and lower layers, the density and thickness of the uppermost layer, the gravitational acceleration, and the impact velocity. If the cohesion difference ΔY_0 is sufficient (>50–450 kPa for an impact velocity of 12.7 km/s, which translates to a $\Delta C > 0.03$–0.27), CCs may form for essentially any strength contrast (at least as low as a factor of 2) between the two target layers. Such low strength contrasts may be caused by any small strength discontinuity in the shallow subsurface of the Moon. Consequently, CCs may not necessarily be an indication of the prominent lunar regolith-mare interface.
2. Two parameters control the progressive change in crater morphologies as a function of crater diameter: (1) the minimum impact velocity (U_{min}) and (2) the material strengths of the layers (ΔC). Three morphological scenarios are possible in function of crater diameter (Figure 16): (1) for $U < U_{min}$, NC morphology transitions to FBC, to CC, and finally back to NC morphology, which resembles the transition sequence previously observed in early laboratory experiments (Q&O); (2) for $U > U_{min}$ and a limited collapse in the upper layer, a transition from normal directly to concentric morphology occurs at $D_{RIM}/T = 5.0$–6.5; (2*) for $U > U_{min}$ and a large collapse in the upper layer, the onset of the transition from normal directly to concentric morphology occurs only at greater $D_{RIM}/T = 9.0$–11.0 due to stronger modification at late stage; (3) for large impact velocity $U \gg U_{min}$, targets that do not have a sufficiently high strength difference, that have rather gradual variations in target properties, or/and that have a too thin upper layer, only NC

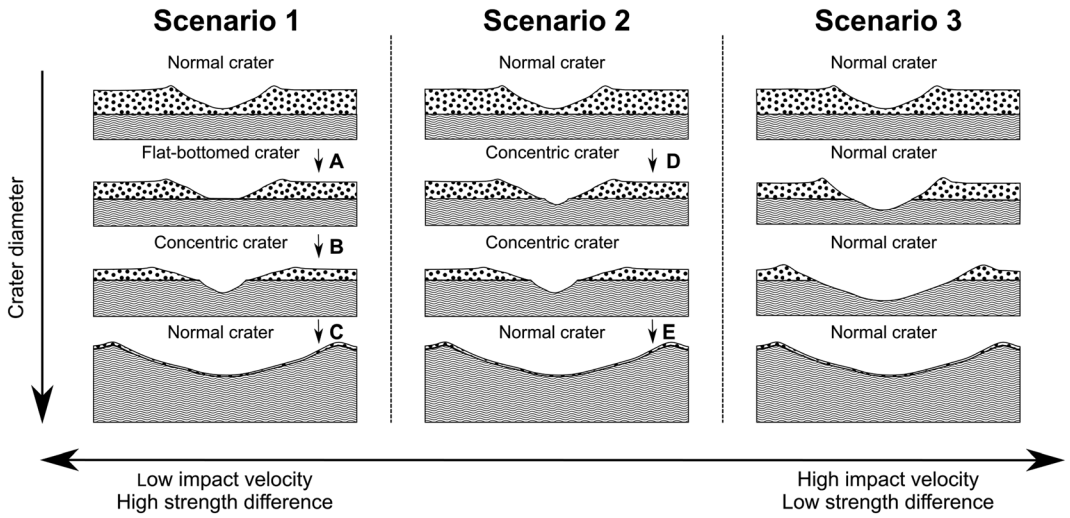

Figure 16. Sketch representation of the three possible morphological scenarios as function of crater diameter, impact velocity, and strength difference between layers. The bold letters represent a particular transition between crater morphologies. Based on our numerical results with varying cohesion differences ΔY_0 = 0–99.9 MPa, friction coefficients, and impact velocities U = 1.0–12.7 km/s, we found that the transition A occurs at relative thickness D_{RIM}/T = 4–5, B at D_{RIM}/T = 5–16, C at D_{RIM}/T = 20–23, D at D_{RIM}/T = 5.0–11.0, and E at D_{RIM}/T = 12–19.

geometries form. In scenario 1, the transition from NC to FBC occurs at D_{RIM}/T = 4.0–5.0, whereas the transition from FBC to CC can occur between D_{RIM}/T = 5.0–16.0 depending on the specific target properties. However, this behavior is limited to high substrate strength and low-impact velocities and therefore most relevant for secondary lunar cratering and low-velocity impacts. A transition from normal directly to concentric morphology (and back to normal) is more abundant in our numerical results, however, and represents the more typical scenario of larger and higher velocity impacts.

3. Due to variations in the progressive change of crater morphology as a function of impact energy, the transitions to CC morphology (normal to concentric and flat-bottomed to concentric) are observed over a wide range of relative layer thickness (D_{RIM}/T = 5–16). This stands in contrast to early laboratory experiments (Q&O), which did not consider the full range of target strengths relevant for the lunar and other planetary surfaces. Such large variations of the transition onset described by D_{RIM}/T challenge the interpretation of crater morphology with regard to lunar regolith thickness. According to our modeling results, the thickness of the lunar regolith estimated from crater morphologies may have an uncertainty of up to a factor of five.
4. The transition to FBC morphology occurs at rather constant relative uppermost layer thickness (D_{RIM}/T = 4.3) for impact velocities ranging from U = 1–12 km/s, regardless of target properties. Consequently, the onset diameter of FBCs may be the most appropriate morphological feature of a crater to derive regolith thickness and may help to better constrain the strength of lunar surface materials at planetary scale and the properties of impacts that formed simple lunar craters (such as their velocity).

Acknowledgments
We are grateful to K. Miljković, M. S. Robinson and E. P. Turtle for their constructive comments, which improved this paper. N. C. P., T. R., and S. C. W. appreciate support from the Research Council of Norway via the 235058/F20 CRATER CLOCK grant and a Centre of Excellence grant to the Centre of Earth Evolution and Dynamics (CEED, 223272) as well as an IS-DAAD mobility grant (NFR 244761/F11). K. W. was supported by the IS-DAAD mobility grant 57159947 and was funded by German Research Foundation grants WU 355/6-2 and SFB-TRR 170 (A4), Pub #34. All calculations have been performed on STALLO, a Notur high-performance computing facility at the University of Tromsø under project IDs nn9283 and nn9010. We would like to acknowledge the developers of iSALE and pySALEplot (G. S. Collins, K. Wünnemann, D. Elbeshausen, B. A. Ivanov, H. J. Melosh, and T. Davison). Details regarding iSALE are available at www.isale-code.de. Supporting information can be found in the online version.

References

Amsden, A. A., Ruppel, H. M., & Hirt, C. W. (1980). SALE: A simplified ALE computer program for fluid flow at all speeds, Los Alamos Natl. Lab. Rep., LA-8095 (101 pp.).

Bart, G. D., Nickerson, R. D., Lawder, M. T., & Melosh, H. J. (2011). Global survey of lunar regolith depths from LROC images. *Icarus*, *215*(2), 485–490. https://doi.org/10.1016/j.icarus.2011.07.017

Basilevsky, A. T., Kreslavsky, M. A., Karachevtseva, I. P., & Gusakova, E. N. (2014). Morphometry of small impact craters in the Lunokhod-1 and Lunokhod-2 study areas. *Planetary and Space Science*, *92*, 77–87. https://doi.org/10.1016/j.pss.2013.12.016

Brown, H. M., Awumah, A. A., Henriksen, M. R., Manheim, M. R., Cisneros, E., Wagner, R. V., & Robinson, M. S. (2017). Ames Steteo Pipeline and LROC ASU Digital Terrain Model (DTM) comparison, in 3rd Planetary Data Workshop 2017.

Collins, G. S. (2014). Numerical simulations of impact crater formation with dilatancy. *Journal of Geophysical Research: Planets*, *119*, 2600–2619. https://doi.org/10.1002/2014JE004708

Collins, G. S., Melosh, H. J., & Ivanov, B. A. (2004). Modeling damage and deformation in impact simulations. *Meteoritics and Planetary Science*, *39*(2), 217–231. https://doi.org/10.1111/j.1945-5100.2004.tb00337.x

Collins, G. S., Melosh, H. J., & Wünnemann, K. (2011). Improvements to the ϵ-α porous compaction model for simulating impacts into high-porosity solar system objects. *International Journal of Impact Engineering*, *38*(6), 434–439. https://doi.org/10.1016/j.ijimpeng.2010.10.013

Daubar, I. J., Atwood-Stone, C., Byrne, S., McEwen, A. S., & Russell, P. S. (2014). The morphology of small fresh craters on Mars and the Moon. *Journal of Geophysical Research: Planets*, *119*, 2620–2639. https://doi.org/10.1002/2014JE004671

Fa, W., & Jin, Y. (2009). A primary analysis of microwave brightness temperature of lunar surface from Chang-E 1 multi-channel radiometer observation and inversion of regolith layer thickness. *Icarus*, *207*, 605–615. https://doi.org/10.1016/j.icarus.2009.11.034

Fa, W., Liu, T., Zhu, M. H., & Haruyama, J. (2014). Regolith thickness over Sinus Iridum: Results from morphology and size-frequency distribution of small impact craters. *Journal of Geophysical Research: Planets*, *119*, 1914–1935. https://doi.org/10.1002/2013JE004604

Fassett, C. I. (2016). Analysis of impact crater populations and the geochronology of planetary surfaces in the inner solar system. *Journal of Geophysical Research: Planets*, *121*, 1900–1926. https://doi.org/10.1002/2016JE005094

Fassett, C. I., & Thomson, B. J. (2014). Crater degradation on the lunar maria: Topographic diffusion and the rate of erosion on the Moon. *Journal of Geophysical Research: Planets*, *119*, 2255–2271. https://doi.org/10.1002/2014JE004698

Gault, D. E., Quaide, W. L., & Oberbeck, V. R. (1966). Interpreting ranger photographs from impact cratering Studies. In W. N. Hess (Ed.), *The Nature of the Lunar Surface* (pp. 125–140). Baltimore, MD: The Johns Hopkins Press.

Grieve, R. A. F., & Garvin, J. B. (1984). A geometric model for excavation and modification at terrestrial simple impact craters. *Journal of Geophysical Research*, *89*(B13), 11,561–11,572. https://doi.org/10.1029/JB089iB13p11561

Holsapple, K. A. (1993). The scaling of impact processes in planetary sciences. *Annual Review of Earth and Planetary Sciences*, *21*(1), 333–373. https://doi.org/10.1146/annurev. ea. 21.050193.002001

Holsapple, K. A., & Schmidt, R. M. (1982). On the scaling of crater dimensions: 2. Impact processes. *Journal of Geophysical Research*, *87*(B3), 1849–7256. https://doi.org/10.1029/JB087iB03p01849

Ivanov, B. A., Deniem, D., & Neukum, G. (1997). Implementation of dynamic strength models into 2D hydrocodes: Applications for atmospheric breakup and impact cratering. *International Journal of Impact Engineering*, *20*(1-5), 411–430. https://doi.org/10.1016/S0734-743X(97)87511-2

Kiefer, W. S., Macke, R. J., Britt, D. T., Irving, A. J., & Consolmagno, G. J. (2012). The density and porosity of lunar rocks. *Geophysical Research Letters*, *39*, L07201. https://doi.org/10.1029/2012GL051319

Kneissl, T., van Gasselt, S., & Neukum, G. (2011). Map-projection-independent crater size-frequency determination in GIS environments—New software tool for ArcGIS. *Planetary and Space Science*, *59*(11–12), 1243–1254. https://doi.org/10.1016/J.PSS.2010.03.015

Mahanti, P., Robinson, M. S., Thompson, T. J., & Henriksen, M. R. (2017). Small lunar craters at the Apollo 16 and 17 landing sties—Morphology and degradation. *Icarus*, *299*, 475–501.

McKay, D. S., Heiken, G., Basu, A., Blanford, G., Simon, S., Reedy, R., et al. (1991). The lunar regolith. In G. H. Heiken, D. T. Vaniman, & B. M. French (Eds.), *Lunar Sourcebook: A User's Guide to the Moon* (pp. 285–356). Cambridge: Cambridge University Press.

Melosh, H. J. (1977). Crater modification by gravity: A mechanical analysis of slumping. In D. J. Roddy, R. O. Pepin, & R. B. Merrill (Eds.), *Impact and Explosion Cratering* (pp. 1245–1260). New York: Pergamon Press.

Melosh, H. J., Ryan, E. V., & Asphaug, E. (1992). Dynamic fragmentation in impacts: Hydrocode simulation of laboratory impacts. *Journal of Geophysical Research*, *97*(E9), 14,735–14,759. https://doi.org/10.1029/92JE01632

Muehlberger, W. R., Batson, R. M., Boudette, E. L., Duke, C. M., Eggleton, R. E., Elston, D. P., et al. (1972). Preliminary investigation of the Apollo 16 landing site. In *Apollo 16 Preliminary science report, NASA Special Paper 315* (pp. 6-1–6-81). Washington, DC: U.S. Government Printing Office.

Muehlberger, W. R., Batson, R. M., Cernan, E. A., Freeman, V. L., Hait, M. H., Holt, H. E., et al. (1973). Preliminary geologic investigation of the Apollo 17 landing site. In *Apollo 17 preliminary science report, NASA Special Paper 330* (pp. 6-1–6-71). Washington, DC: U.S. Government Printing Office.

Oberbeck, V. R., & Quaide, W. L. (1967). Estimated thickness of a fragmental surface layer of Oceanus Procellarum. *Journal of Geophysical Research*, *72*(18), 4697–4704. https://doi.org/10.1029/JZ072i018p04697

Oberbeck, V. R., & Quaide, W. L. (1968). Genetic implications of lunar regolith thickness variations. *Icarus*, *9*(1-3), 446–465. https://doi.org/10.1016/0019-1035(68)90039-0

Oberbeck, V. R., Quaide, W. L., Mahan, M., & Paulson, J. (1973). Monte Carlo calculations of lunar regolith thickness distributions. *Icarus*, *19*(1), 87–107. https://doi.org/10.1016/0019-1035(73)90141-3

Piekutowski, A. J. (1977). Cratering mechanisms observed in laboratory-scale high explosive experiments. In D. J. Roddy, R. O. Pepin, & R. B. Merrill (Eds.), *Impact and Explosion Cratering* (pp. 67–102). New York: Pergamon Press.

Pierazzo, E., Artemieva, N. A., & Ivanov, B. A. (2005). Starting conditions for hydrothermal systems underneath Martian craters: Hydrocode modeling. *Geological Society of America Special Papers*, *384*, 443–457. https://doi.org/10.1130/0-8137-2384-1.443

Prieur, N. C., Rolf, T., Luther, R., Wünnemann, K., Xiao, Z., & Werner, S. C. (2017). The effect of target properties on transient crater scaling for simple craters. *Journal of Geophysical Research: Planets*, *122*, 1704–1726. https://doi.org/10.1002/2017JE005283

Quaide, W. L., & Oberbeck, V. R. (1968). Thickness determinations of the lunar surface layer from lunar impact craters. *Journal of Geophysical Research*, *73*(16), 5247–5270. https://doi.org/10.1029/JB073i016p05247

Richardson, J. E., Melosh, H. J., & Greenberg, R. (2004). Impact-induced seismic activity on asteroid 433 Eros: A surface modification process. *Science*, *306*(5701), 1526–1529. https://doi.org/10.1126/science.1104731

Richardson, J. E., Melosh, H. J., Greenberg, R. J., & O'Brien, D. P. (2005). The global effects of impact-induced seismic activity on fractured asteroid surface morphology. *Icarus*, *179*(2), 325–349. https://doi.org/10.1016/j.icarus.2005.07.005

Robinson, M. S., Brylow, S. M., Tschimmel, M., Humm, D., Lawrence, S. J., Thomas, P. C., et al. (2010). Lunar Reconnaissance Orbiter Camera (LROC) instrument overview. *Space Science Reviews*, *150*(1-4), 81–124. https://doi.org/10.1007/s11214-010-9634-2

Roddy, D. J. (1977). Large-scale impact and explosion craters: Comparisons of morphological and structural analogs. In D. J. Roddy, R. O. Pepin, & R. B. Merrill (Eds.), *Impact and Explosion Cratering* (pp. 185–246). New York: Pergamon Press.

Schmidt, R. M. (1980). Meteor crater: Energy of formation—Implications of centrifuge scaling. In *Lunar Planetary Science Conference 11th* (pp. 2099–2128). Houston, TX.

Schmidt, R. M., & Housen, K. R. (1987). Some recent advances in the scaling of impact and explosion cratering. *International Journal of Impact Engineering*, *5*(1-4), 543–560. https://doi.org/10.1016/0734-743X(87)90069-8

Schmitt, H. H. (1973). Apollo 17: Report on the Valley of Taurus-Littrow. *Science*, *182*(4113), 681–690. https://doi.org/10.1126/science.182.4113.681

Schultz, R. A. (1995). Limits on strength and deformation properties of jointed basaltic rock masses. *Rock Mechanics and Rock Engineering*, *28*(1), 1–15. https://doi.org/10.1007/BF01024770

Senft, L. E., & Stewart, S. T. (2007). Modeling impact cratering in layered surfaces. *Journal of Geophysical Research: Planets*, *112*, E11002. https://doi.org/10.1029/2007JE002894

Shoemaker, E. M., Batson, R. M., Bean, A. L., Conrad, C. Jr., Dahlem, D. H., Goddard, E. N., et al. (1970). Preliminary geologic investigation of the Apollo 12 landing site, part A. In *Apollo 12 preliminary science report, NASA Special Paper 235* (pp. 113–156). Washington, DC: U.S. Government Printing Office.

Slyuta, E. N. (2014). Physical and mechanical properties of the lunar soil (a review). *Solar System Research*, *48*(5), 330–353. https://doi.org/10.1134/S0038094614050050

Stöffler, D., Gault, D. E., Wedekind, J., & Polkowski, G. (1975). Experimental hypervelocity impact into quartz sand: Distribution and shock metamorphism of ejecta. *Journal of Geophysical Research*, *80*(29), 4062–4077. https://doi.org/10.1029/JB080i029p04062

Stopar, J. D., Robinson, M. S., Barnouin, O. S., Mcewen, A. S., Speyerer, E. J., Henriksen, M. R., & Sutton, S. S. (2017). Relative depths of simple craters and the nature of the lunar regolith. *Icarus*, *1157*, 0–1. https://doi.org/10.1016/j.icarus.2017.05.022

Swann, G. A., Bailey, N. G., Batson, R. M., Freeman, V. L., Hait, M. H., Head, J. W., et al. (1972). Preliminary investigation of the Apollo 15 landing site. In *Apollo 15 preliminary science report, NASA Special Paper 289* (pp. 5-1–5-112). Washington, DC: U.S. Government Printing Office.

Watters, W. A., Hundal, C. B., Radford, A., Collins, G. S., & Tornabene, L. L. (2017). Dependence of secondary crater characteristics on downrange distance: High-resolution morphometry and simulations. *Journal of Geophysical Research: Planets*, *122*, 1773–1800. https://doi.org/10.1002/2017JE005295

Wieczorek, M. A., Neumann, G. A., Nimmo, F., Kiefer, W. S., Taylor, G. J., Melosh, H. J., et al. (2013). The crust of the Moon as seen by GRAIL. *Science*, *339*(6120), 671–675. https://doi.org/10.1126/science.1231530

Wilcox, B. B., Robinson, M. S., Thomas, P. C., & Hawke, B. R. (2005). Constraints on the depth and variability of the lunar regolith. *Meteoritics and Planetary Science*, *40*(5), 695–710. https://doi.org/10.1111/j.1945-5100.2005.tb00974.x

Wood, C. A. (1978). Lunar concentric craters. In *Lunar Planetary Science Conference 9th* (pp. 1264–1266). Houston TX.

Wünnemann, K., Collins, G. S., & Melosh, H. J. (2006). A strain-based porosity model for use in hydrocode simulations of impacts and implications for transient crater growth in porous targets. *Icarus*, *180*(2), 514–527. https://doi.org/10.1016/j.icarus.2005.10.013

Xiao, Z., Zeng, Z., Ding, N., & Molaro, J. (2013). Mass wasting features on the Moon—How active is the lunar surface? *Earth and Planetary Science Letters*, *376*, 1–11. https://doi.org/10.1016/j.epsl.2013.06.015

Yamamoto, S., Wada, K., Okabe, N., & Matsui, T. (2006). Transient crater growth in granular targets: An experimental study of low velocity impacts into glass sphere targets. *Icarus*, *183*(1), 215–224. https://doi.org/10.1016/j.icarus.2006.02.002